NSTX FY2011 Year End Report: Facility and Diagnostics

NSTX started the FY 2011 plasma operation in Oct. 2010 to take advantage of the excellent operational conditions prevailing at the conclusion of the very successful experimental campaign in FY 2010. The early FY 2011 plasma operation conducted high priority experiments addressing the FY 2011 joint research target and other FY 2011 research milestones. While this experimental campaign was short, it was highly productive scientifically as will be described below. In FY 2011, the NSTX facility operated for 4.21 run weeks, producing 839 plasma shots. The ~200 plasma shots per week achieved was a record indicating an excellent operational efficiency. The facility then embarked on the planned outage to implement additional facility and diagnostics enhancements including those supported under the ARRA funding. All the in-vessel upgrade installation tasks were completed on schedule (as described below) in May 2011. After a three-week high temperature bakeout, the NSTX facility performed the standard integrated systems test procedure (ISTP) to prepare for the resumption of plasma operation. However, on July 20, 2011, during this ISTP, a turn-to-turn electrical short occurred within the toroidal field (TF) coil inner bundle. The TF bundle had then been operating without any detectable issues for 20,000 plasma shots for over more than 7 years of plasma operation. The subsequent removal and investigation of the damaged TF bundle revealed that the cause of the electrical short was a gradual deterioration of the insulation between TF conductors which had become contaminated by residues of a flux used during the soft soldering operation at the time of the TF bundle fabrication in 2003. There were no signs of TF bundle deterioration due to mechanical and thermal cycles. This finding was examined and accepted by a panel of external magnet experts which conducted an independent TF failure review on September 7, 2011. Rather than repairing the damaged TF bundle, which would have take about 1 year of down time, the NSTX team decided to request to proceed directly to the planned NSTX Upgrade Project outage, which was originally scheduled to start on April 1, 2012. This early outage start will accelerate the NSTX Upgrade Project schedule by about six months, enabling the NSTX to start the post upgrade operation in mid-FY 2014 instead of the planned FY 2015 start. In the light of the finding on the cause of the TF failure, a number of improvements were recommended and will be implemented for the manufacturing of the new TF bundle for the NSTX Upgrade.

Summary descriptions of the results of facility, and diagnostic milestones are provided below. Other NSTX information and statistics such as publications, invited talks, colloquium presentations, awards, and leadership are reported elsewhere.

Base Facility and Diagnostics Achievements for FY2011

Facility Milestones for FY2011

Facility Milestone F(11-1): Operate NSTX Facility for 14 Experimental Run Weeks (Target - September 2011, 4.21 run weeks completed – October 2010)

Milestone Report: For FY 2011, NSTX achieved 4.21 run weeks with 839 plasma shots on October 25, 2010. This represents a record ~ 200 plasma shots per run week. The remainder of the FY 2011 run weeks were not completed due to an electrical failure in the toroidal field (TF) coil inner bundle which occurred on July 20, 2011 during the integrated systems testing routinely

performed prior to restarting plasma operation. It should be noted that the TF failure occurred after more than 20,000 pulses of the coil conducted over more than 7 years since its installation. The subsequent investigation of the damaged TF revealed that the cause of the failure was an electrical short circuit between two neighboring conductors. It was determined that the failure was due to a gradual deterioration of the conductor insulation which had been contaminated by residues of a flux containing zinc-chloride. This flux was used during fabrication of the TF bundle in 2003 while soft-soldering the water cooling tube into a groove in the TF conductor. Although the conductor was thoroughly cleaned after the soldering operation, residual flux trapped within the solder apparently seeped into the insulation material during the curing of the B-stage epoxy insulation which was performed at ~160°C. This finding was endorsed by a panel of external experts in magnet construction which conducted an independent review of the TF failure on September 7, 2011. After carefully assessing options, the NSTX project decided not to repair the TF coil but to request to proceed directly to the planned NSTX Upgrade Project outage, which was originally scheduled to start on April 1, 2012. Repairing the original TF bundle would have taken about 1 year of down-time. This early start on the NSTX Upgrade Project should result in an acceleration of its schedule by about six months. In light of the findings concerning the failure of the original TF bundle, a number of improvements will be implemented in manufacturing the new TF bundle for the upgrade, including eliminating the use of zinc-chloride based flux, to help prevent insulation failures.

Diagnostic Milestones for FY2011

Diagnostic Milestone D(11-1): Complete the commissioning of a real-time plasma velocity (RTV) diagnostic system (September 2011, Completed – September 2011)

Description: The NSTX charge-exchange recombination spectroscopy (CHERS) system, which provides detailed toroidal velocity profile evolution information between plasma discharges, is not currently capable of providing real-time information which will be needed for control of the plasma rotation profile. In FY2011, the system will be equipped with new four channel detectors and a fast data acquisition system to enable real-time analysis of plasma rotation data.

Milestone Report:

A Real-Time Velocity (RTV) diagnostic was installed on NSTX to measure the plasma toroidal velocity with high temporal resolution. The real-time velocity data will be incorporated into the plasma control system for feedback control of the plasma rotation profile using the NBI and non-resonant magnetic braking as the actuators. The diagnostic, based on active charge-exchange recombination spectroscopy (CHERS), can measure at up to six radial locations with a maximum sampling rate of 5 kHz. The RTV system uses two toroidally separated views to distinguish the CVI emission from the region intercepting the heating NB from the background (intrinsic) contribution. The system uses fixed-wavelength spectrometers coupled to fast CCD cameras (see Figure D11-1(a)) to provide the high sampling rate needed for real-time control. Acquisition of camera data by a computer and its analysis within a total time interval under 200μs, including the read-out, background subtraction and fitting of multiple gaussian components to the measured line shape, was demonstrated. A scheme for conveying the analyzed data to the NSTX plasma control system using its existing data acquisition hardware was developed and tested. The spectrometer wavelength calibration was established by observing spectral lines close in

wavelength to the CVI line from a Ne glow discharge run in the NSTX vacuum chamber. An example spectrum measured on two channels during Ne glow plasma in NSTX is shown in Figure D11-1(b).

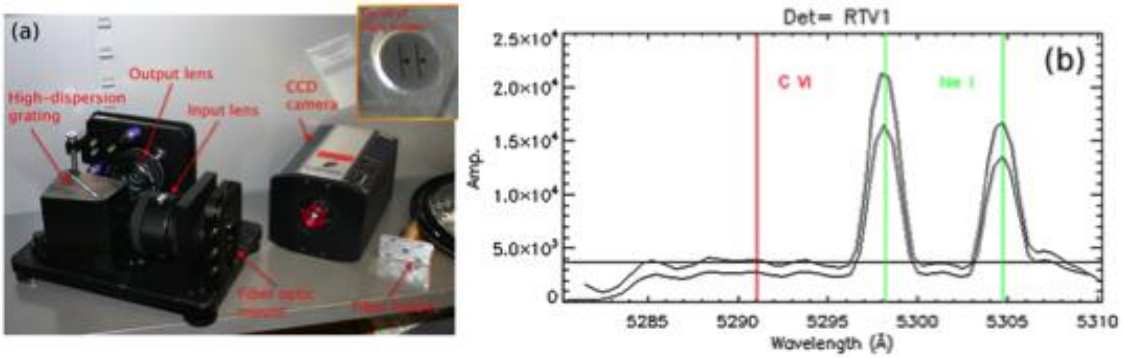

Figure D11-1: *(a) the RTV hardware (CCD camera, spectrometer) and (b) an example of spectra measured on two channels during a Ne glow*

ARRA Facility and Diagnostics Achievements for FY2011

The ARRA funded diagnostic upgrades include ten additional channels for the multi-pulse Thomson scattering system for improved H-mode pedestal and plasma edge spatial resolution to support the FY2011 Joint Research Milestone, and the Motional Stark Effect Laser-Induced Fluorescence advanced diagnostic system for internal magnetic and electric field measurements which will also provide important data for the FY2011 Joint Research Milestone. The facility upgrades include an enhancement to the lithium liquid divertor (LLD) capability for improved divertor pumping to control edge collisionality for the FY2011 Joint Research Milestone, a second switching power amplifier (SPA) to provide flexible spatial spectra of the applied 3-D field perturbations to control error fields, resistive wall modes and resonant magnetic perturbation which will contribute to the FY2011 Joint Research Milestone. The LLD enhancements included the replacement of graphite tiles with molybdenum tiles on the inboard side of the lower divertor. These new tiles were fabricated and installed in March 2011 as shown in Fig. F11-1. The split-top molybdenum on SS tile design satisfies all the NSTX divertor tile requirements. The molybdenum tiles enables testing of effects of expanded coverage of divertor surfaces with Mo on the effects of lithium coatings, C impurities and CHI non-inductive start-up.

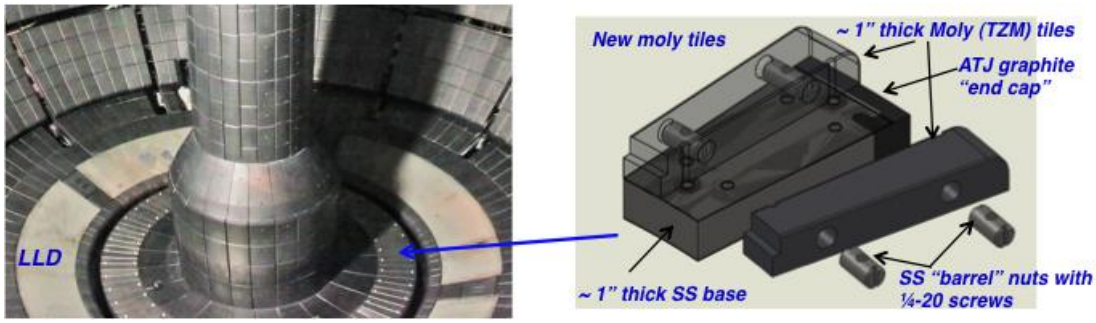

Figure F11-1: *Inboard divertor molybdenum tiles installed in NSTX.*

ARRA Facility Milestones for FY2011

ARRA Facility Milestone AF(11-1): Complete commissioning of facility upgrades. (August 2011, **Completed – July 2011**)

Description: An additional 3-channel Switching Power Amplifier will be installed and commissioned in FY2011 so that each of the six EF/RWM/RMP coils will be separately powered, allowing simultaneous control of the full range of toroidal harmonics of the applied field.

Milestone Report:

An additional 3-channel Switching Power Amplifier was installed and commissioned in FY2011. This allows each of the six non-axisymmetric radial-field perturbation coils on NSTX to be powered independently, thereby providing the capability for simultaneous control of the toroidal harmonics, $n = 0 – 3$, of the applied field perturbations as shown in Fig. F11-2(a). Following the completion of the first four weeks of the 2011 run in October 2010, the power and control cabling and other services for the second SPA were installed over the winter. This newly installed SPA system is shown in Fig. F11-2 (b). The power testing of the rectifier and DC power link from the FCPC power supply hall was completed in March. Following pre-operational testing of the system and the incorporation of changes to the NSTX power supply controller to accommodate the additional SPA commands in its output stream, operation of all six SPA channels powering their respective error-field control coils was achieved in July. The basic software modifications to the higher-level Plasma Control System (PCS) software for operating and controlling the second SPA were then installed and independent programmed control by the PCS of the currents in the six error-field correction coils was demonstrated at the beginning of August, shortly after the failure of the TF coil.

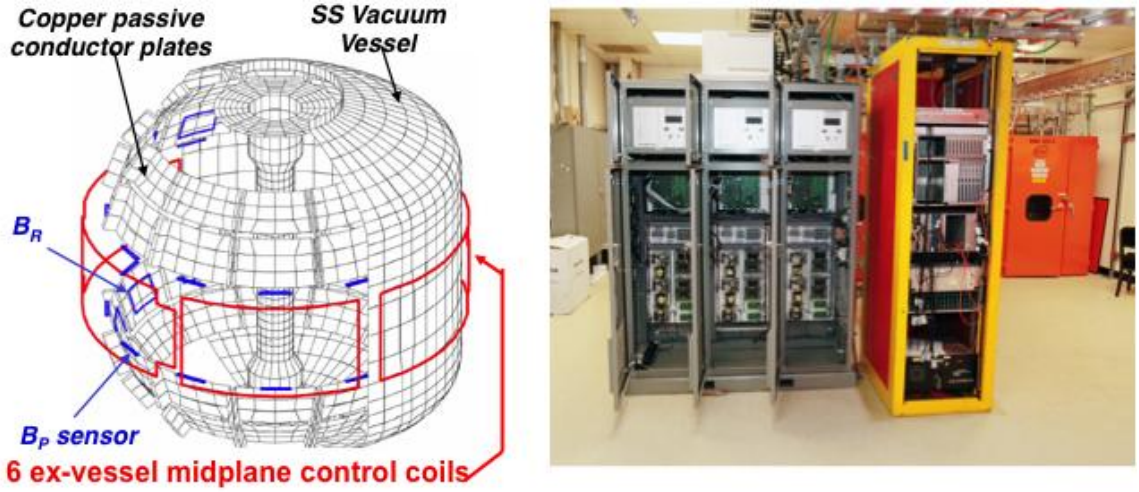

Figure F11-2: *(a) A schematic of six EFC/RWM coils on NSTX. (b). Installed 2nd Switching Power Amplifier (SPA) system to enable all six EFC/RWM coils for control of n = 1, 2, 3 simultaneously.*

ARRA Diagnostic Milestones for FY2011

ARRA Diagnostic Milestone AD(11-1): Complete commissioning of diagnostic upgrades. (August 2011, **Completed – August 2011**)

Description: Ten additional channels for the multi-pulse Thomson scattering system will be installed in FY2011. These channels will be concentrated in the regions of internal transport barriers, the outboard H-mode pedestal, and the plasma scrape off layer where improved spatial resolution is desirable to test theory and modeling of the pedestal and boundary physics relevant for ITER and future ST devices as shown in Fig. AD11-1 (a). The Motional Stark Effect measurement based on Laser Induced Fluorescence (MSE-LIF) diagnostic will provide measurements of the field line pitch angle profile without requiring injection of the heating neutral beam needed for the present MSE system on NSTX which detects collisionally induced fluorescence (MSE-CIF). It will, for example, provide critical data for measuring RF-driven current in NSTX without the competing effect of current driven by the heating neutral beam. Also, direct reconstruction of the total plasma pressure profile should be possible for the first time from its capability to make local measurements of the total magnetic field in the plasma. Combining this measurement with the comprehensive thermal profile measurements already available on NSTX, the fast-ion pressure profile can be inferred and compared to predictions to determine the influence of Alfvén Eigenmodes and other MHD activity on fast-ion confinement. Furthermore, the data from the two MSE systems, MSE-CIF and MSE-LIF, can be combined to calculate the radial electric field profile, an important element in plasma transport research. The MSE-LIF system will be commissioned in FY2011.

Milestone Report:

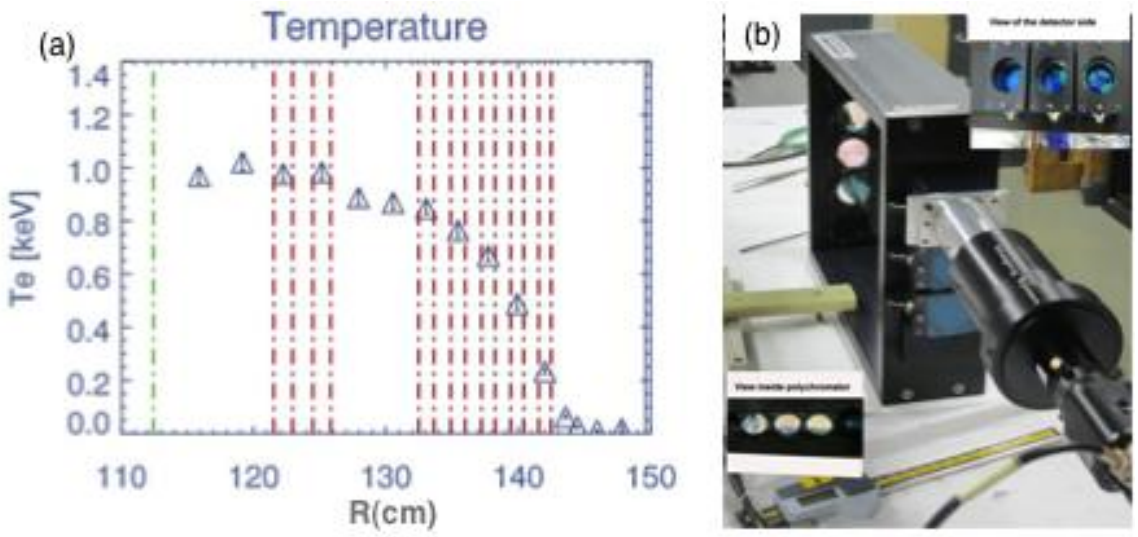

Figure AD11-1: *(a) Extra channels improving the spatial resolution of H-mode pedestal and internal transport barrier regions. (b) A picture of a polychrometer.*

Twelve additional channels for the multi-pulse Thomson scattering (MPTS) system were installed and commissioned in FY2011. After acceptance testing, the new polychromators were first assembled and aligned, and then installed in the MPTS room. A picture of a polychromator is shown in Fig. AD11-1 (b). The optical fiber bundles bringing scattered light from the plasma were then reconfigured to produce the desired spatial distribution of measurement points. The locations of all the MPTS channels were then measured by back-illumination along each fiber of a target plate mounted inside the vacuum vessel.

The spectral transmission curve of each polychromator was then measured with a scanning monochromator and the overall calibration was performed *in situ* by employing Rayleigh and Raman scattering of the light from the MPTS laser system by nitrogen and argon introduced into the vacuum vessel. Measurements of the optical transmission of the observation window were also made to establish a baseline for monitoring its evolution through the run. The upgraded MPTS system with 42 total channels was ready for operation in July at the planned start of the second phase of the 2011 experimental campaign.

In collaboration with researchers from Nova Photonics Inc., the installation and commissioning of the first three channels of the Motional Stark Effect measurement based on Laser Induced Fluorescence (MSE-LIF) was completed in August 2011. A schematic and picture of the MSE-LIF system is shown in Fig. AD11-2. After extensive development and testing in the laboratory, the diagnostic neutral beam, surrounded by a two-layer magnetic shield, was mounted on its stand and connected to the NSTX vacuum vessel, its power supplies and other services. After commissioning its control and interlock systems, operation of the diagnostic neutral beam was achieved. The development of a high-power, narrow-line laser source for excitation of the injected neutrals was completed and the laser was installed. The viewing optics, filters and detectors for 10 sightlines crossing the neutral beam path were designed, procured and installed. Finally, in September, the magnetic field sensitivity of the MSE-LIF system was tested by injecting the neutral beam into deuterium gas introduced into the NSTX vacuum vessel with up to 3mT applied by the poloidal field coils. In this test, the MSE-LIF system was able to distinguish magnetic field changes of less than 1mT.

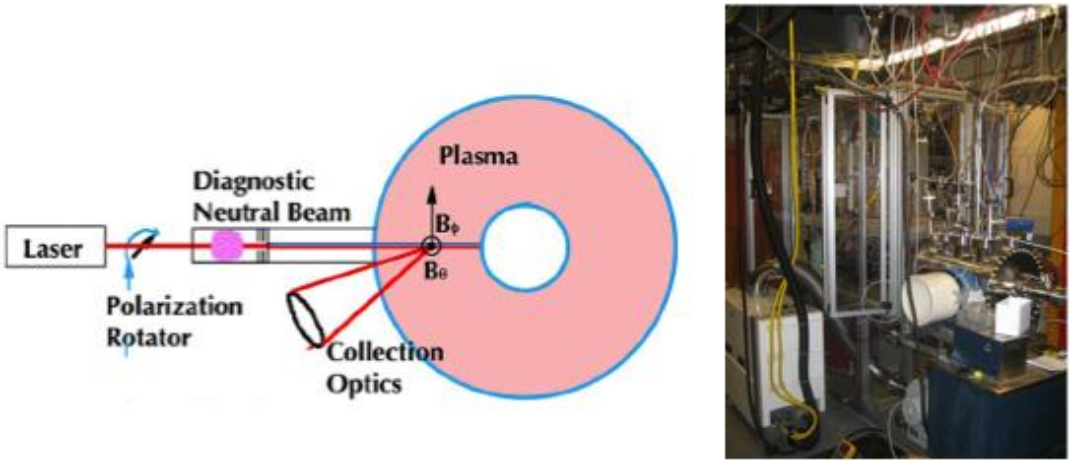

Figure AD11-2: *(a) A schematic of the MSE-LIF system on NSTX. (b) A picture of the MSE-LIF system.*

Other (Non-Milestone) Base Facility and Diagnostics Achievements for FY2011

In addition to the base and ARRA funded facility and diagnostic milestone related upgrades described above, there were a significant number of enhancements performed by the NSTX research team led by the NSTX collaborating institutions. The achievements are described below.

The ORNL boundary physics group has designed and implemented a wide angle, 30 Hz infrared camera system on NSTX this year. A dual-band adapter was also implemented for variable surface emissivity due to lithium films. This system was designed as part of Princeton University student's first year experimental project. In addition, two eroding thermocouples near the PFC tile surface were installed and instrumented. These thermocouples, which have a design response time ~ 1 ms are intended to be used in the future for feedback control of PFC surface temperature in NSTX-Upgrade. Finally a set of 16 new "filterscope" chords were implemented. The gain control and data acquisition is done dynamically via a PC. The units are capable of 100 kHz sampling speeds.

In FY2011, the LLNL collaboration in the diagnostics area on NSTX focused on new and improved measurements for plasma-surface interaction studies with lithium-coated graphite and molybdenum plasma-facing component, as well as divertor impurity and plasma diagnostics. New capabilities included a new vacuum-ultraviolet divertor spectrometer (SPRED) that was brought from LLNL to NSTX to monitor carbon and molybdenum emission in the divertor for impurity and power balance studies. Another new capability intended to support the NSTX lithium program was a new near-infrared spectrometer for divertor molecular and atomic spectroscopy. To provide pilot measurements for radiative divertor control, a new optical Penning discharge chamber was installed in the lower divertor area to provide a way to monitor pressure of deuterium or or gaseous impurities (e.g., argon) that could be injected to increase divertor radiated power. Improvements were also made to other LLNL-supported diagnostics, notably the divertor Lyman-alpha and radiometer array, four one-dimensional filtered CCD arrays, divertor imaging spectrometers, and filterscopes. The goal was to provide routine quantitative emission measurements in the upper and lower divertor areas, as well as the inner outer walls.

In order to investigate Massive Gas Injection (MGI), the most promising method found thus far for safely terminating discharges in ITER, the University of Washington team installed and commissioned high-capacity gas injectors at two different poloidal locations on NSTX. With these, NSTX can offer new data by injecting gas into the private flux and lower x-point regions to determine if this is a more desirable location for massive gas injection. By comparing gas injection from this new location to results obtained from a similar amount of gas injected from the conventional outer mid-plane, NSTX can provide additional insight, new data for improving computational simulations, and additional knowledge to understand disruption mitigation physics.

In FY 2011, the Johns Hopkins University spectroscopy group implemented a high resolution tangential Multi-Energy SXR (ME-SXR) array for an improved diagnostic of the NSTX edge / H-mode pedestal plasma. The diagnostic simultaneously images the peripheral plasma ($0.6<r/a<1$) in five energy bands spanning the range 0.01 – 10 keV, with 1 cm spatial resolution and up to 10 μs time resolution. With detailed emission modeling, the multi-energy technique enables high

resolution and fast measurements of the edge T_e and impurity density profiles, for perturbative studies of the edge impurity and electron transport, ELM physics studies, and improved edge stability calculations. The ME-SXR array is complemented by a tangential Transmission Grating Imaging Spectrometer (TGIS) that measures with few cm spatial resolution and few Å spectral resolution the XUV impurity line emission, for an additional constraint in the modeling of the ME-SXR profiles. For the 2011 run the edge ME-SXR array was made fully operational with a total of 96 chords and its noise immunity increased. The TGIS was upgraded in spatial and spectral resolution and its efficiency calibrated in the laboratory and at a synchrotron light source. The edge ME-SXR diagnostic had been first tested during FY11 using neon puffs and shown excellent capability for high resolution impurity transport measurements. The first assessment of edge transport in a 5.5 kG, beam-heated ELM-free H-mode, indicated neon diffusivity ranging from 0.5±0.25 m^2/s at r/a=0.6, to 2.5±0.5 m^2/s at r/a=0.9, consistent with our previous estimates and with NCLASS predictions. In addition, integration of the ME-SXR data with the TGIS data shows that a quite accurate picture of the low- to high- Z impurity content can be obtained using the two combined diagnostics. The high resolution ME-SXR data revealed also new interesting phenomena in the NSTX boundary, such as a reduction in impurity density before a type-I ELM and the formation of slow, cm-sized, impurity rich filaments.

The UC Davis group improved the far-infra-red interferometer and polarimeter (FIReTIP) system so that is could be utilized for the NSTX density feedback control in FY 2011. A system for humidity control was successfully installed and tested. Measurements made with FIReTIP of phenomena accompanying the EPH-mode have been analyzed to be presented in the H-mode workshop. For FY2011, the UCLA Diagnostics Group fabricated and delivered a single-channel radial polarimeter/interferometer on a Bay G midplane port on NSTX. The diagnostic operates at a frequency of 288 GHz and utilizes a flat center-stack tile as a retroreflecting target. The system can be configured as either a polarimeter or an interferometer. In addition to the investigation of magnetic and current equilibria, the wide bandwidth of the system (f>2 MHz) allows it to be used for diagnosing density and/or magnetic fluctuation associated with a wide range of instabilities, including low frequency MHD (e.g. NTM's), Alfven eigenmodes, and microtearing modes.

Led by the University of Wisconsin group, the Beam Emission Spectroscopy diagnostic system was upgraded from the 16 channel system, which had been commissioned and utilized in many experiments on NSTX in 2010, to a 32 channel system. This upgraded BES system was successfully implemented in July 2011.

NSTX FY2011 Year End Report: Research Results

In FY2011, the NSTX research team contributed experimental data and analysis in support of the 2011 DOE Joint milestone*: "Improve the understanding of the physics mechanisms responsible for the structure of the pedestal and compare with the predictive models described in the companion theory milestone. Perform experiments to test theoretical physics models in the pedestal region on multiple devices over a broad range of plasma parameters (e.g., collisionality, beta, and aspect ratio). Detailed measurements of the height and width of the pedestal will be performed augmented by measurements of the radial electric field. The evolution of these parameters during the discharge will be studied. Initial measurements of the turbulence in the pedestal region will also be performed to improve understanding of the relationship between edge turbulent transport and pedestal structure."*

The NSTX contributions to the 2011 Joint Milestone are described in a separate report.

Summary descriptions of the results of research milestones are provided below. Descriptions of additional selected research highlights are also provided.

FY2011 Research Milestone R(11-1): Measure fluctuations responsible for turbulent electron, ion and impurity transport (Target - September 2011. Completed – September 2011)

Milestone Description: The thermal transport scalings of electrons and ions with magnetic field and plasma current in NSTX H-mode plasmas have been found to be different from those of high-aspect-ratio tokamaks. Furthermore, recent experiments show that lithiated wall conditions can affect global confinement of NSTX H-mode plasmas and lead to different scalings with magnetic field and plasma current from un-lithiated plasmas. High-k scattering measurements have identified ETG turbulence as one candidate for the anomalous electron energy transport for both H and L-mode plasmas. However, low-k fluctuations and fast-ion-driven modes, e.g. GAE, may also contribute to electron transport. Furthermore, low-k fluctuations may also contribute significantly to momentum, ion thermal, and particle/impurity transport. In addition to measuring high-k fluctuations, the low-k turbulence and fast-ion-driven modes will be measured with a Beam Emission Spectroscopy (BES) diagnostic. Additional low-k fluctuation measurements will be made using the upgraded reflectometer, interferometer, and gas puff imaging systems. The turbulence k spectrum will be measured as function of plasma parameters and coupled with power balance analysis. Experiments on particle transport will be carried out by using gas puffs coupled with density measurements and low-k to high-k turbulence measurements. Impurity transport will be studied by coupling impurity puff and edge SXR measurements.

Milestone R(11-1) Report:

The BES diagnostic was implemented in FY2010 and has been utilized to measured low-k fluctuations in a variety of discharge scenarios. Low-k fluctuations decrease at the LH transition, but fluctuations can subsequently increase as the H-mode phase evolves as shown in Figure R11-1-1 and reported previously.

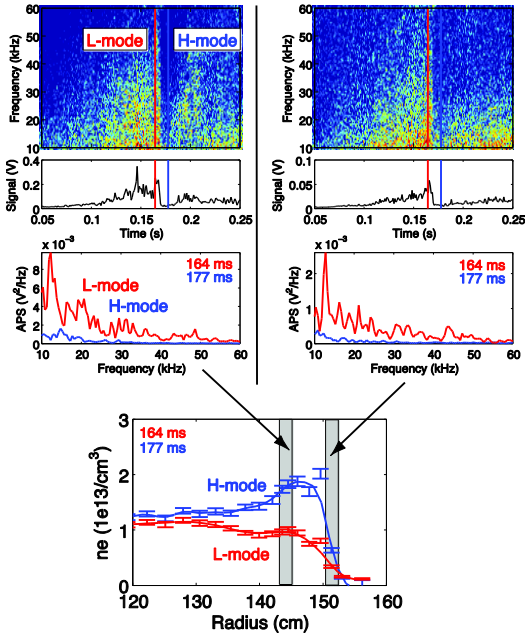

Figure R11-1-1: *Low-k turbulence fluctuations measured with the BES diagnostic at two spatial locations near the plasma edge in the low confinement mode (L-mode) phase and just after the transition to the high-confinement mode (H-mode).*

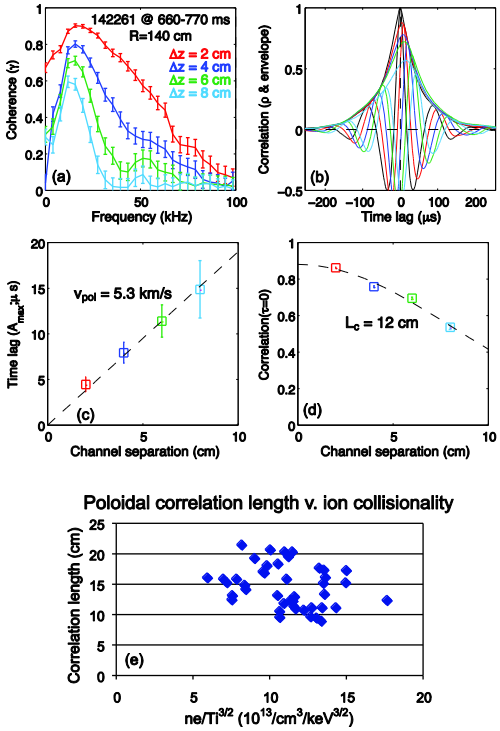

Figure R11-1-2: *(a) Coherence spectra and (b) time-lag cross-correlation calculations for poloidally-separated channels at R=140 cm provide time-lag and correlation quantities. (c) Time-lag at peak correlation v. channel separation provides the advection velocity and (d) correlation at zero time-lag v. channel separation provides the correlation length. (e) Computed correlation length v. collisionality.*

In FY2011, a database of correlation lengths has been assembled to better understand low-k turbulence trends in ST plasmas. Broadband spectra can extend to 100 kHz, and the database obtained using BES data at R=140 cm (r/a~0.85) indicates poloidal correlation lengths are generally 10-20 cm. Poloidal correlation lengths in stationary H-mode discharges increase at higher n_e, n_e gradient, and T_e gradient, and q/ŝ (ŝ is the normalized magnetic shear) and decrease at higher T_i and T_i gradient. Early in the H-mode phase, poloidal correlation lengths can exhibit different scalings. For example, poloidal correlation lengths increase at higher T_i and decrease at lower q/ŝ early in the H-mode phase. The change in scalings during the H-mode phase indicates different turbulent modes may be active at different times in the discharge. Coherence calculations, time-lag analysis, and correlation lengths are shown in Figure R11-1-2(a-d). As shown in Figure R11-1-2(e), preliminary calculations indicate poloidal correlation lengths at R=140 cm in stationary H-mode periods (B_T = 4.4 kG, I_P = 900 kA, and P_{NBI} = 4 MW) decrease modestly at higher ion collisionality.

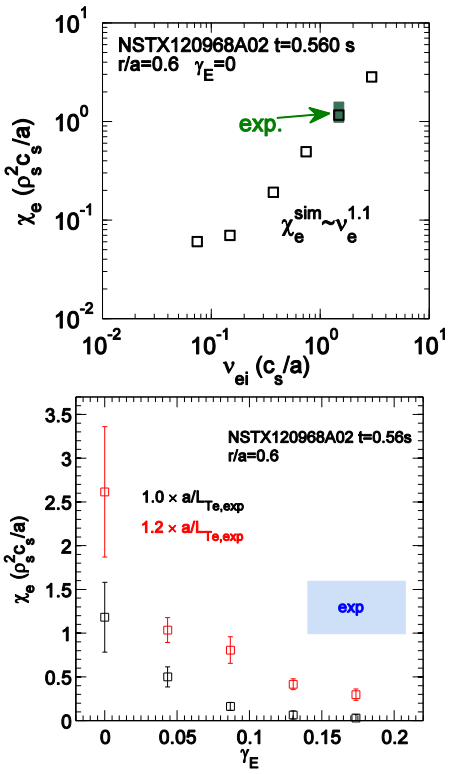

Figure R11-1-3: *(Top) Predicted χ_e vs. ν_{ei} (log-log scale), and(bottom) E×B shear rate, γ_E (c_s/a). The shaded regions indicate experimental values with uncertainties.*

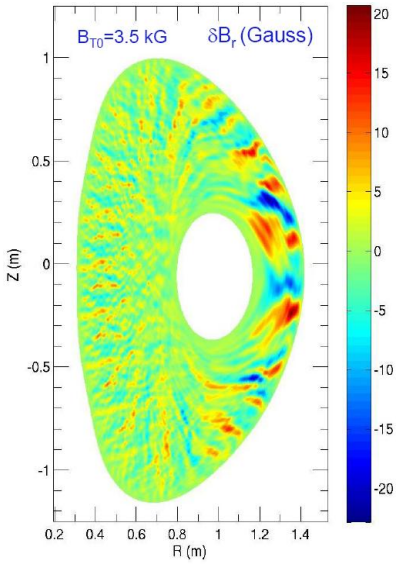

Figure R11-1-4: *Magnetic field perturbations for the micro-tearing simulations.*

NSTX has also made substantial progress in understanding a potentially important cause of the anomalous electron transport in ST plasmas. In particular, researchers on NSTX have recently obtained the first comprehensive nonlinear gyrokinetic simulations of microtearing (MT) turbulence using the GYRO code based on a high ν_* NSTX discharge [R11-1-1] that predict significant electron thermal transport comparable to experimental analysis (χ_e~5 m^2/s at r/a=0.6). Additional simulations have shown the scaling with collisionality, $\chi_e \sim \nu_{*e}^{1.1}$ (Fig. R11-1-3) is remarkably similar to expectations from global confinement scaling $\Omega\tau_E \sim \nu_*^{-0.95}$ [R11-1-2], suggesting it may be an important contributor to anomalous electron transport. This simple interpretation is complicated by the fact that microtearing transport is very "stiff", varying ±~100% for ±20% changes in a/L_{Te}, while being significantly suppressed with experimental levels of E×B shear (Fig. R11-1-3). Ongoing simulations show the strength and scaling of transport is also influenced by resolution requirements and must be investigated further for more accurate quantitative predictions.

Linear calculations have been used to determine qualitative scaling expectations over broader parameter scans which can be used to distinguish it from other instabilities. For example, in the high-ν_* discharge studied above, the normalized experimental gradient a/L_{Te} is found to be about 2-3× the linear microtearing threshold in the region of r/a=0.5-0.8 (holding all other parameters fixed). In these cases the large values of Z_{eff}~2.5-3 completely stabilize the ETG mode, but are weakly destabilizing to MT. In this same region, MT growth rates increase with magnetic shear and decrease with safety factor (limited to the range s/q≈0.5-1.5), again opposite to ETG stability expectations. The MT threshold depends on β_e, as increasing β_e is generally destabilizing. MT stability also depends uniquely on electron collisionality, with a maximum growth rate occurring for a ratio of ν_{ei}/ω_{*e}~3-5, decreasing at both lower and higher collisionalities. Variation of these parameters can be used as experimental knobs in an attempt to discriminate when ETG or MT should be dominant. Development of a unifying expression for microtearing threshold and scaling of instability strength is in progress

(guided by theoretical expectations [R11-1-3]), and will be used to develop and validate reduced transport models.

Unique from traditional electrostatic modes (ITG, TEM, ETG), magnetic perturbations from micro-tearing turbulence are spatially broad on the outboard side with large local amplitude $\delta B_r/B$~0.5% (Figure R11-1-4). Modeling was used to show the feasibility of measuring micro-tearing mode magnetic fluctuations in NSTX with a 288 GHz radial chord polarimeter. The sensitivity of the polarimeter to the micro-tearing modes was assessed using a 1-D model of electromagnetic (EM) wave propagation [R11-1-4] in conjunction with the GYRO simulation of micro-tearing modes in NSTX described above. The polarimeter launches a plane polarized EM wave with a rotating polarization. The vertical component of the electric field—sinusoidally amplitude modulated because of the rotation—is detected upon exiting the plasma. Modeling shows that the radial magnetic field fluctuations of the micro-tearing modes (Figure R11-1-4) cause Faraday rotation, resulting in ~ 1—2° phase fluctuations. This is well within the capability of the polarimeter, which has been demonstrated to have sub-degree phase resolution in laboratory tests. While Faraday rotation also depends on plasma density in principle, the modeling shows that micro-tearing mode density fluctuations contribute very little to the phase fluctuations. This is primarily due to the geometry of the measurement, but also to the short radial scale of the micro-tearing mode density fluctuations. Thus, in summary, these synthetic diagnostic simulations of the Faraday and Cotton-Mouton effects indicate that a radially-integrated polarimetry measurement near the midplane should be sensitive to NSTX micro-tearing perturbations [R11-1-4]. This diagnostic was set to be installed by the UCLA group for the FY11-12 run campaign, and a dedicated experiment was allocated to investigate ν_* scaling of these measurements at high β and Z_{eff} where MT should dominate over other instabilities.

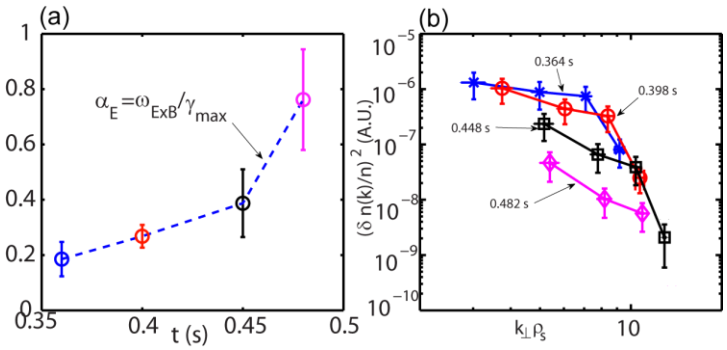

Figure R11-1-5: *(a) The ratio between the ExB shear rate and the maximum linear growth rate for ITG instability; (b)* $\boldsymbol{k}_\perp$ *spectra in arbitrary unit at the four corresponding time points as in (a).*

Another leading candidate micro-instability potentially responsible for anomalous electron transport is the ETG mode. In FY2011, ETG studies were extended using the high-k microwave scattering diagnostic to perform studies of the effects of rotation shear on high-k turbulence. Equilibrium ExB shear has been predicted to quench ion-scale turbulence when $\omega_{E\times B} \approx 0.5\gamma_{max}$ where $\omega_{E\times B}$ is the ExB shear rate and γ_{max} is the mode maximum linear growth rate [R11-1-5]. Experimental observations have shown that equilibrium ExB shear could suppress electron-scale turbulence as well [R11-1-6], where electron-scale turbulence is measured by a 280 GHz microwave scattering system (the high-k scattering system) with a fine radial localization of ±2 cm [R11-1-7]. However, due to limitations in scattering configuration, the change in spectral shape was not explored in Ref. [R11-1-6] with only a single k measurement. Here, with improved scattering schemes, we are able to present first experimental observation of k spectrum change as the ExB shear rate is continuously increased. The observation was made in shot 141716, a NSTX NBI-

heated L-mode plasma with toroidal field of 5.5 kG, plasma current of 900 kA, where 2 MW NB was first injected from 90 ms to 230 ms and then re-injected from 300 ms to the end of the discharge. During the second phase of NBI, the plasma toroidal rotation speed started to increase continuously, which leads to simultaneous increase in the ExB shear rate in the outer half of the plasma. The high-k scattering system was configured to measure electron-scale turbulence for a $k_\perp \rho_s$ range of 2 to about 14 at about R≈139 to 143 cm (r/a≈0.67-0.73). In Fig. R11-1-5(a), we plot $\alpha_E = \omega_{E\times B}/\gamma_{max}$, where $\omega_{E\times B}$ is calculated using the definition in Ref. [R11-1-5] and γ_{max} is the maximum linear growth rate for ITG instability calculated with GS2 code [R11-1-8]. Note that the gradual increase of α_E from t=0.36 s to 0.45 s is due to the increase of $\omega_{E\times B}$ while the sharper increase of α_E after t= 0.45 s is due to both the increase of $\omega_{E\times B}$ and decrease of γ_{max}. The measured $k_\perp$ spectra at corresponding time points same as in Fig. R11-1-5(a) are shown in Fig. R11-1-5(b). It can be easily seen that from t=0.364 s to 0.398 s the $k_\perp$ spectra have only small changes while α_E increases from about 0.2 to 0.26. Large decrease in spectral power at $k_\perp \rho_s < 10$ occurs while α_E approaches 0.4. It is interesting to note that the k spectra preserve its shape at $k_\perp \rho_s > 10$ for t < 0.48 s only beyond which the spectral power at $k_\perp \rho_s > 10$ also starts to decrease. This further decrease may be due to the large α_E (≈0.8) achieved at t=0.48 s. We also note that ETG instability is also unstable from all times and its growth rate far exceeds the ExB shear rate. Thus we think that some of the observed high-k electron-scale turbulence is nonlinearly driven by low-k ion-scale turbulence and its power decreases as ion-scale turbulence is suppressed by the ExB shear. Finally we note that plasma thermal confinement is also improved in correlation with the turbulence reduction: τ_E increases from 20 ms at t≈0.36 s to about 55 ms at t≈0.48 s.

Alfvénic instabilities have previously been shown to be associated with increased electron thermal and particle transport in the core of NSTX neutral beam-heated H-mode plasmas. Using a recently upgraded 16-channel array of fixed frequency reflectometers, global (GAE) and compressional (CAE) Alfvén eigenmode structures were measured for the first time in the core of an NSTX high-power (6 MW) beam-heated H-mode plasma [R11-1-9] (Figure R11-1-6a). High frequency AE activity has been observed to correlate with enhanced electron thermal transport observed in such plasmas by Stutman *et al.* [R11-1-10]. The high frequency AEs were identified as GAEs and posited to cause the enhanced transport. Notably, the observed CAE structure is strongly core-localized, indicating CAEs are candidates for causing the enhanced transport for the same reasons as the GAEs. Also using the upgraded reflectometer array, toroidicity-induced Alfvén eigenmode (TAE) structure (Figure R11-1-6b) was measured with greatly improved spatial sampling. Measurements of the TAE phase (Figure R11-1-6c), the first in NSTX, show strong radial variation near the midplane, indicating radial propagation caused by non-ideal MHD effects.

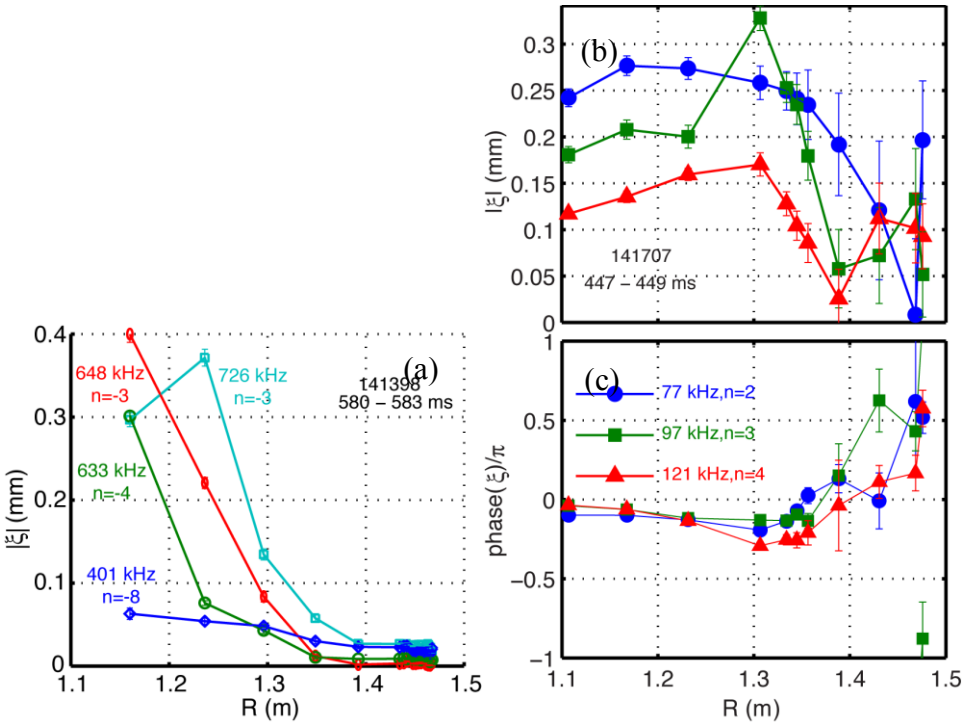

Figure R11-1-6*: a) Radial structure of GAE (f=40 kHz) and CAEs (f=633, 648, 726 kHz); b) radial structure of TAEs and c) TAE phase vs. radius.*

Finally, initial impurity transport measurements using new edge ME-SXR diagnostics are described in the report on R11-4 below, and edge turbulence measurements during L-H transitions using new Doppler backscattering measurements are described in the section on boundary physics highlights.

References

[R11-1-1] W. Guttenfelder et al., Phys. Rev. Lett. **106**, 155004 (2011)
[R11-1-2] S.M. Kaye et al., Nucl. Fusion **47**, 499 (2007)
[R11-1-3] N.T. Gladd et al., Phys. Fluids **23**, 1182 (1980)
[R11-1-4] J. Zhang, et al., 2010 *Rev. Sci. Ins.* **81** 10D519, J. Zhang et al., TTF, San Diego (2011), http://ttf2011.pppl.gov/Presentations.htm
[R11-1-5] R.E. Waltz and R.L. Miller, Phys. Plasmas 6, 4265 (1999)
[R11-1-6] D.R. Smith et al., Phys. Rev. Lett. 102, 225005 (2009)
[R11-1-7] D. R. Smith et al., Rev. Sci. Instrum. 79, 123501 (2008)
[R11-1-8] M. Kotschenreuther, G. Rewoldt, W.M. Tang, Comput. Phys. Comm. 88, 128 (1995)
[R11-1-9] N.A. Crocker, et al., *Plasma Phys. Control. Fusion* **53** (2011) 105001
[R11-1-10] D. Stutman, et al., *Phys. Rev. Lett.* **102** (2009) 115002

FY2011 Research Milestone (R11-2): R(11-2): Assess ST stability dependence on plasma aspect ratio and boundary shaping. (Target - September 2011. Completed – September 2011)

Milestone Description: Next-step ST conceptual designs assume aspect ratio $A \geq 1.6$ and/or high elongation (κ = 3-3.5) to maximize projected fusion performance. These aspect ratio and elongation values are higher than commonly accessed on NSTX ($A < 1.5$ and κ = 2.4-2.8), and to narrow this gap, NSTX Upgrade is designed to overlap next-step configurations by operating with higher aspect ratio (A=1.6-1.7) and κ up to 3. This combination of increased aspect ratio and higher elongation is projected to increase vertical instability growth rates by up to a factor of 3 and degrade kink marginal stability normalized beta by -0.5 to -1 relative to present NSTX performance. In this milestone, the integrated plasma scenarios previously developed in NSTX will be extended to plasma geometries closer to those of the Upgrade and next-step devices and the stability properties systematically explored. The maximum sustainable normalized beta will be determined versus aspect ratio (up to A=1.7) and elongation (up to 3) and compared to ideal stability theory using codes such as DCON and PEST. Both passive and actively-controlled RWM stability will be assessed both experimentally and theoretically using codes such as MISK and VALEN, and the viability of previously developed control techniques will be tested. The vertical stability margin will also be determined, and vertical motion detection and control improvements will be implemented. Boundary shape parameters (including squareness) will be varied to assess the impact of shaping and plasma-wall coupling on global stability. Edge NTV rotation damping is also expected to vary with aspect ratio and will be investigated. Plasma profile modifications and the impact on NSTX integrated performance (confinement, non-inductive fraction, pedestal stability, and recycling and divertor dynamics) will also be documented. Overall, these results will help guide stability control development for both NSTX Upgrade and next-step STs.

Milestone R(11-2) Report:

Experiments were conducted during the 4-week FY2011 run to study the impact of aspect ratio and elongation on the integrated performance of NSTX plasmas. The base configuration for these experiments was the standard high-triangularity fiducial/reference discharge, shown in black in Figure R11-2-1. The current in the divertor coils PF-1A U&L was then increased, causing the inner plasma-wall gap to become larger. This results in an increase to both the aspect ratio and the elongation. The blue curve in Figure R11-2-1 shows the plasma boundary for the highest A and κ shape. Also shown is the PFC boundary for NSTX-Upgrade, indicating that the larger-A shape is nearly representative of plasmas to be made in NSTX-Upgrade.

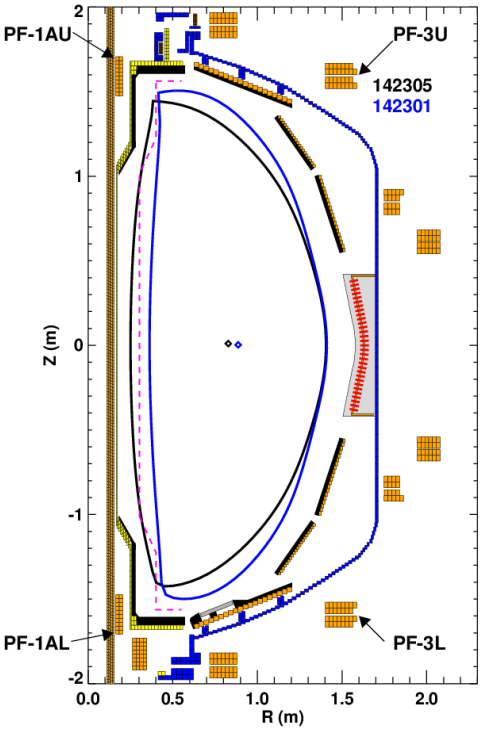

Figure R11-2-1: *Plasma boundaries for a typical high-elongation discharge (142305), and a high aspect ratio and elongation discharge (142301). Also shown in magenta is the inboard side PFC boundary for NSTX-Upgrade.*

Calculations and measurements were done in order to understand the impact of this shape variation on global stability. With regard to n=1 stability, calculations of the n=1 ideal MHD no-wall stability limit were completed for a series of experimental plasmas with varying aspect ratios; these calculations utilized measured kinetic and current profiles. The result is shown in Figure R11-2-2. The red points represent the calculated β_N limit, and show a significant decrease as the aspect ratio is increased. The magnitude of the change is similar to that found it previous theoretical studies [R11-2-1], but with a lower actual value due to the profile optimizations used in that study. The blue points show achieved β_N values for these discharges; NSTX has sustained β_N ~4.4 at A=1.65 for many wall times. Importantly, the experiment was operated at a fixed moderate heating power, so that the disruptive β_N limit would not be reached during the scan. The actual experimental β_N limit is thus some unknown amount larger than these achieved levels. These β_N levels are sufficient to meet the goals of 100% non-inductive current drive for extended pulses in NSTX-U.

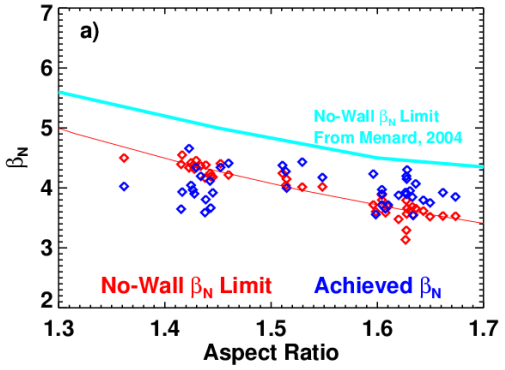

Figure R11-2-2: *Achieved normalized beta (blue) and calculated no-wall stability limit (red) vs. aspect ratio for an NSTX experimental aspect ratio scan. The no-wall limit assuming optimized profiles is shown in light blue.*

With regard to n=0 stability, NSTX conducted experiments "freezing" the vertical control system and measuring the plasma vertical motion and displacement growth-rate. An increase in the n=0 growth rate by a factor of ~2.5 was observed as the aspect ratio increased from 1.4 to 1.65. It was also observed that the A > 1.6 discharges tended to lose vertical position control for l_i > 0.65. Both of these observations are consistent with a reduction in the n=0 stability for higher aspect ratio, where the "natural elongation" is reduced. Despite the increased vertical instability growth rates at increased aspect ratio, Figure R11-2-3 shows that access to very high elongation near 3 at increased aspect ratio is possible in NSTX (and in NSTX Upgrade) [R11-2-2] as required for a range of proposed next-step ST-based devices.

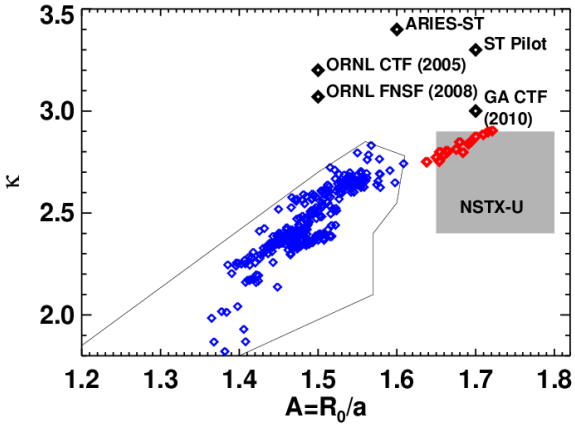

Figure R11-2-3: *Space of elongation versus aspect ratio for NSTX discharges. The black line encloses the historical NSTX operating space for discharges with flat-top duration exceeding 0.5 s, and specific high-performance discharges are indicated in blue. The points collected in the high aspect-ratio experiment are indicated in red. The approximate NSTX Upgrade operating space is indicated in a grey box, and the parameters of a few next-step ST design, are indicated with black diamonds.*

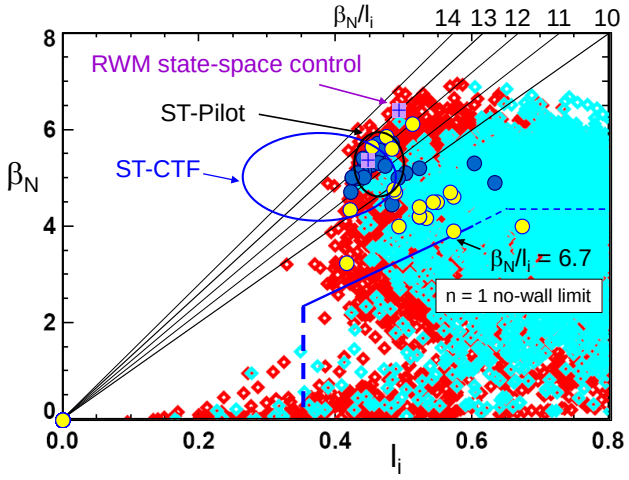

Figure R11-2-4: *High β_N attained at low l_i in NSTX appropriate for future ST devices. Red/cyan points indicate plasmas with/without n=1 active RWM control. Blue circles indicate stable long pulse plasma with active RWM control; yellow indicates disruptions.*

In addition to investigating the ideal stability limits and vertical control limits of increased aspect ratio plasmas with shaping closer to next-step spherical torus (ST) fusion applications (e.g. a component test facility [R11-2-3], or pilot power plant [R11-2-4]), studies were also performed to assess operation at sustained high normalized beta, $\beta_N \equiv 10^8 <\beta_t> aB0/I_p$, ($\beta_t \equiv 2\mu_0 <p>/B_0^2$) and reduced internal inductance characteristic of high bootstrap current fraction plasmas. While low l_i operation is favorable increased elongation and efficient non-inductive operation, it is generally unfavorable for global MHD mode stability, reducing the ideal n = 1 no-wall beta limit, $\beta_N^{no\text{-}wall}$. NSTX operation has demonstrated high β_N operation with l_i typically in the range 0.6 < l_i < 0.8, with $\beta_N^{no\text{-}wall}$ computed by the DCON code to be 4.2 – 4.4 [R11-2-5].

NSTX has more recently demonstrated transient β_N > 6.5 and β_N / l_i > 13.5, and pulse-averaged β_N (averaged over the period of constant plasma current), $<\beta_N>_{pulse}$ > 5.5 in low l_i plasmas in the range 0.4 < l_i < 0.6 with active n =1 mode control (Figure R11-2-4). Pulse-averaged values of (l_i,

β_N) now intercept the higher l_i portion of the planned operational ranges for ST-CTF and ST Pilot plants.

Especially important is that the ideal n = 1 no-wall stability limit is significantly reduced at these low l_i values, so that β_N now exceeds the DCON computed $\beta_N^{no\text{-}wall}$ for equilibrium reconstructions of these plasmas by up to a factor of two. In addition, synthetic variations of the pressure profile for plasmas with $l_i \sim 0.38$ show these equilibria to be at the purely current-driven ideal kink stability limit, as they are computed to be ideally unstable at all values of $\beta_N > 0$.

In this operational regime, passive or active kink and resistive wall mode (RWM) stabilization is therefore critical. Two new control approaches are investigated in NSTX. First, combined use of radial and poloidal field RWM sensors in proportional gain control provided feedback on n = 1 modes. The disruption probability due to unstable RWMs was reduced from 48% in initial low l_i experiments to 14% with this control, but remarkably, the reduced disruption probability was

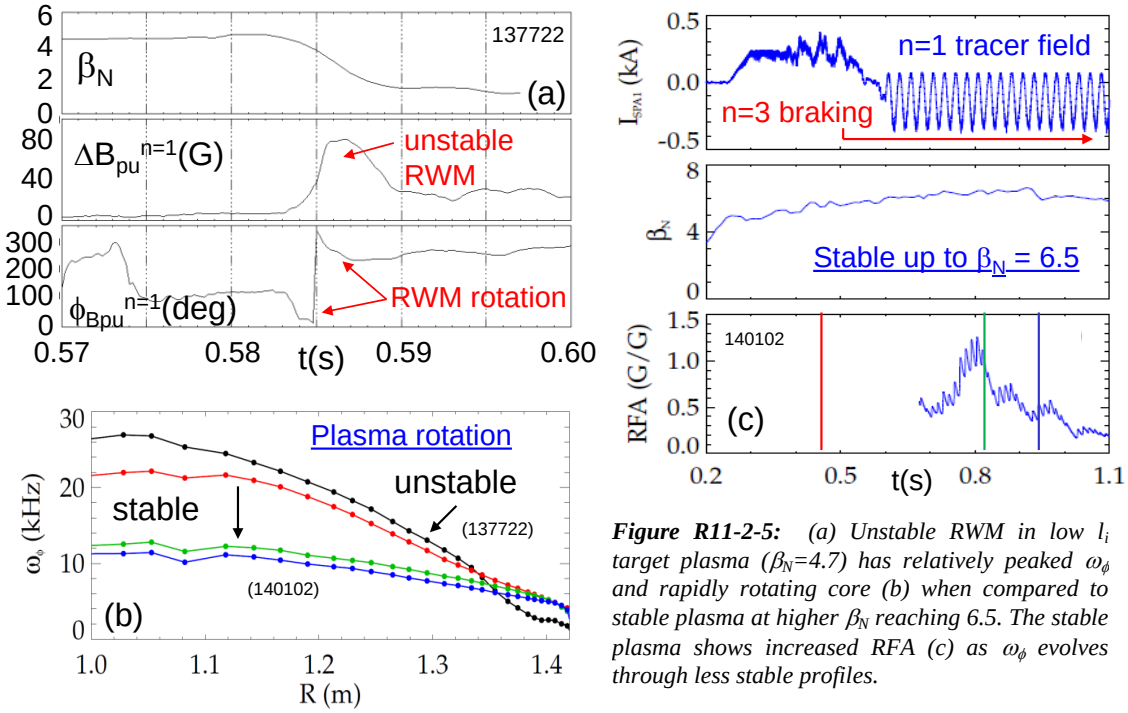

Figure R11-2-5: *(a) Unstable RWM in low l_i target plasma (β_N=4.7) has relatively peaked ω_ϕ and rapidly rotating core (b) when compared to stable plasma at higher β_N reaching 6.5. The stable plasma shows increased RFA (c) as ω_ϕ evolves through less stable profiles.*

observed mostly in plasmas at high $\beta_N / l_i > 11$ (Figure R11-2-4). Disruptions occurred more frequently at lower β_N. This behavior is examined in Figure R11-2-5 for low l_i plasmas with varying plasma toroidal rotation profiles, ω_ϕ. The RWM unstable plasma at β_N = 4.7 has the highest core rotation, while stable long-pulse plasmas with less peaked ω_ϕ have exceeded β_N = 6.5. Active MHD spectroscopy [R11-2-6] of the stable plasma (Figure R11-2-5c) shows an increase in resonant field amplification (RFA) of an applied n=1 AC tracer field, indicating a closer approach to RWM marginal stability. Greater instability seen at lower β_N / l_i is consistent with decreased RWM stabilization at intermediate plasma rotation levels caused by the profile falling between stabilizing ion precession drift and bounce resonances [R11-2-7-9].

The second approach for improved RWM stabilization is a newly-implemented RWM state-space controller using a state derivative feedback algorithm [R11-2-10] (described previously in the

FY2010 NSTX milestone research report), and incorporating currents due to the RWM unstable eigen-function and those induced in nearby 3D conducting structure by the applied control field and plasma response. Testing this physics is especially important for ITER [R11-2-11] and high neutron wall loading devices where greater control coil shielding will be needed. Using a number of states equal or greater than required by Hankel singular value (HSV) analysis (7 in this case) provides sufficient 3D conducting structure current detail to match experimental sensors with greater fidelity during RWM activity. This controller was used for RWM stabilization producing long-pulse plasmas (limited by coil heating constraints) reaching near maximum values of $\beta_N / l_i =$ 13.4 (See Figure R11-2-4).

Beyond RWM active control research, studies have also been performed investigating the passive stability and dispersion relation of the RWM, and the predicted RWM stability trends at reduced collisionality. Such studies are important since the expected reduction in collisionality in NSTX Upgrade and next-step STs could potentially modify RWM stability in important ways. Theory for the stability of the RWM that includes kinetic effects arising from perturbation of the distribution function of particles has been developed [R11-2-12] and successfully compared with experimental results [R11-2-7-14]. In particular, resonances between thermal particle motions and the plasma rotation can lead to a dissipation of the mode energy while energetic particles (EPs) can provide a restoring force that resists the expansion of the magnetic field. The resulting RWM dispersion relation allows for multiple roots of the instability, which were recently investigated using the MISK code [R11-2-15]. Additionally, the treatment of particle collisions was recently shown to be an important factor in stability calculations [R11-2-16].

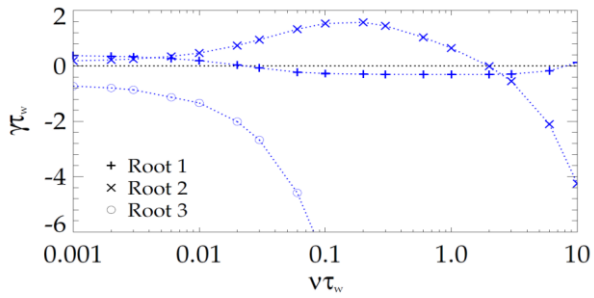

Figure R11-2-6: *Growth rate of the roots of the RWM dispersion relation, vs. collisionality for an analytic calculation.*

The RWM dispersion relation with kinetic effects is cubic, so three distinct modes of instability could simultaneously exist [R11-2-15, 17]. A detailed examination, however, found that only one root has a slow mode rotation frequency [R11-2-15]. This is the usual RWM mode which is observed in NSTX. The other two modes were found to rotate on the order of the plasma rotation frequency [R11-2-15]. Moreover, these two rotating modes are damped by ion and electron collisions, respectively, and so are predicted to be quite stable in NSTX (Figure R12-2-6). NSTX-U will have a lower collisionality than NSTX, which means that multiple roots of the RWM dispersion relation may be near marginal stability and rotating at moderate frequencies, more like slowly rotating RWMs ($<\tau_w^{-1}$), rather than highly rotating ($>\tau_w^{-1}$), highly damped modes.

Collisions have been shown to have a different impact on RWM stability through kinetic models than through previous models [R11-2-16]. Specifically, collisions are stabilizing by dissipating the mode energy, but are also destabilizing as they reduce the resonant kinetic stabilizing effects. When the plasma rotation frequency is away from a stabilizing resonance (with the precession drift or bounce motions of the thermal particles) the net effect is that collisions have little impact on stability. When kinetic rotational resonances are present, however, low collisionality allows them to be even stronger so that NSTX-U, with lower collisionality, may be more stable than

NSTX, if the plasma rotation is strongly in resonance with thermal particle motion, and there is sufficient energetic particle stabilization as well. Figure R11-2-7 shows an example calculation of the RWM growth rate for an NSTX plasma with the experimental levels of rotation and collisionality scaled. When the rotation is in resonance with the precession drift frequency of thermal ions (roughly at $\omega_\varphi / \omega_\varphi^{exp} = 0.5$), lower collisionality leads to greater stability; otherwise collisionality has little effect on stability.

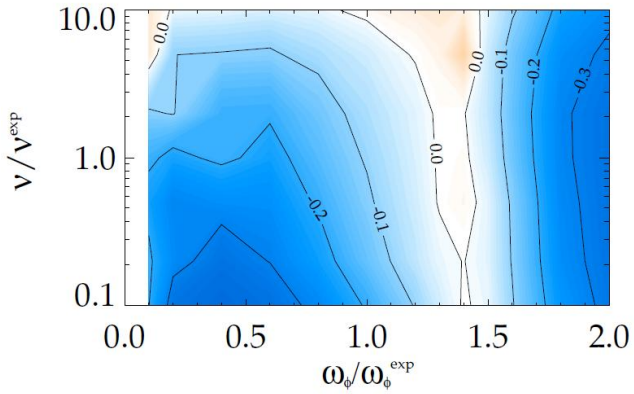

Figure R11-2-7: *Contour plot of normalized growth rate $\gamma\tau_w$ vs. scaled plasma rotation frequency and collisionality for an NSTX plasma. Blue is stable and red is unstable.*

This makes it especially important to avoid off-resonance conditions in NSTX-U operation, and therefore to accurately understand and predict the thermal particle resonant stabilization. The difference between collisionless, energy-independent collisionality, and energy-dependent collisionality can be significant [R11-2-16]. For example the kinetic effects from electrons can be significant in the collisionless case, but are greatly reduced with a proper collisionality model. Further improvements to the collisionality model can be made, including possibly using a pitch-angle dependent Lorentz collisionality, or a momentum-conserving Krook operator. It will also be desirable to have a source of controllable momentum input to reach a favorable rotation profile, and active RWM control to avoid disruptions when the plasma moves away from the resonance condition.

References

[R11-2-1] J.E. Menard, et al., Phys. Plasmas **11**, 639 (2004)
[R11-2-2] S.P. Gerhardt, et al., Nucl. Fusion **51**, 073031 (2011)
[R11-2-3] Y.-K. M. Peng, et al., Plasma Phys. Controll. Fusion **47**, B263 (2005)
[R11-2-4] J.E. Menard, et al., Nucl. Fusion **51** (2011) 103014
[R11-2-5] S.A Sabbagh, A.C. Sontag, J.M. Bialek, et al., Nucl. Fusion **46**, 635 (2006)
[R11-2-6] H. Reimerdes, Chu MS, Garofalo AM, et al., Phys. Rev. Lett. **93**, 135002 (2004)
[R11-2-7] J.W. Berkery, S.A. Sabbagh, R. Betti, et al., Phys. Rev. Lett. **104**, 035003 (2010)
[R11-2-8] S.A. Sabbagh, J.W. Berkery, R.E. Bell, et al., Nucl. Fusion **50**, 025020 (2010)
[R11-2-9] J.W. Berkery, S.A. Sabbagh, R. Betti, et al., 38th European Physical Society Conference on Plasma Physics, Strasbourg, France 2011, paper P1.078
[R11-2-10] T. H. S. Abdelaziz, and M. Valasek, in *16th IFAC World Congress*, edited by P. Zitek (International Federation of Automatic Control, Czech Republic, 2005)
[R11-2-11] O. Katsuro-Hopkins, J.M. Bialek, D.A. Maurer, et al., Nucl. Fusion **47**, 1157 (2007)
[R11-2-12] B. Hu, R. Betti, and J. Manickam, Phys. Plasmas **12**, 057301 (2005)
[R11-2-13] J. Berkery, S. Sabbagh, H. Reimerdes, *et al.*, Phys. Plasmas **17**, 082504 (2010)
[R11-2-14] H. Reimerdes, J. Berkery, M. Lanctot, *et al.*, Phys. Rev. Lett. **106**, 215002 (2011)
[R11-2-15] J. Berkery, S. Sabbagh, H. Reimerdes, *et al.*, Phys. Plasmas **18**, 072501 (2011)
[R11-2-16] J. Berkery, S. Sabbagh, R. Betti, *et al.*, Phys. Rev. Lett. **106**, 075004 (2011)

FY2011 Research Milestone R(11-3): Assess very high flux expansion divertor operation. (Target - September 2011. Completed – September 2011)

Milestone Description: The exploration of high flux expansion divertors for mitigation of high power exhaust is important for NSTX-Upgrade, proposed ST and AT-based fusion nuclear science facilities and for Demo. In this milestone, high flux expansion divertor concepts, e.g. the "snowflake", will be assessed. The magnetic control, divertor heat flux handling and power accountability, pumping with lithium coatings, impurity production, and their trends with engineering parameters will be studied in this configuration. Potential benefits of combining high flux expansion divertors with gas-seeded radiative techniques and ion pumping by lithium will be explored. Two dimensional fluid codes, e.g. UEDGE, will be employed to study divertor heat and particle transport and impurity radiation distribution. Further, H-mode pedestal stability, ELM characterization, as well as edge transport will also be studied in the experiment and modeled with pedestal MHD stability codes, e.g., ELITE, and transport codes, e.g. TRANSP and MIST. This research will provide the foundation for assessing the extrapolability of high flux expansion divertors for heat-flux mitigation in next-step devices.

Milestone R(11-3) Report:

Recent experimental results obtained with a snowflake divertor (SFD) configuration [R11-3-1, 2, 3, 4] demonstrate that this novel divertor geometry may not only hold promise for the outstanding pedestal, ELM and PMI issues, but also can be used as a laboratory for pedestal stability and divertor physics studies in existing tokamaks. In initial NSTX experiments, two divertor coils were used to create and maintain the SFD configurations for periods t =50−150 ms. It was shown that the geometry factors (divertor plasma-wetted surface area, connection length, divertor volume) were significantly increased in the SFD as predicted [R11-3-1], leading to increased volumetric losses, substantial reductions in divertor heat flux, as well as better impurity screening, and a facilitated access to a radiative divertor detachment [R11-3-5, 6].

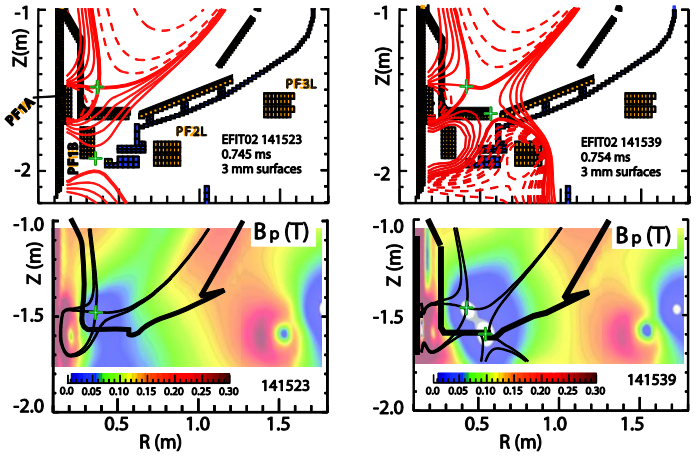

Figure R11-3-1: *A comparison of poloidal magnetic flux equilibria and B_p in the standard divertor and the SFD obtained with three divertor coils in NSTX.*

Magnetic control of the SFD configuration is essential in order to maintain the desired orientation and distance between divertor null-points (Fig. R11-3-1) in a dynamically changing plasma shape. In FY2011, analytic advances in the SFD configuration parametrization [R11-3-7] are being combined with new developments in the NSTX plasma control system [R11-3-8], namely the development of a fast numerical algorithm for locating the multiple null-point positions is being implemented as described below.

In FY2010, the SFD configurations with *three* divertor coils (PF1A, PF1B, and PF2L in Fig. R11-3-1) were designed using a predictive free-boundary axisymmetric Grad-Shafranov equilibrium

solver. The modeling guided the experimental implementation of the three-coil SFD. The steady-state SFD has been obtained for up to 600 ms in highly-shaped 4 MW NBI-heated H-mode plasma discharges of 1.0-1.2 s duration. This enabled a more detailed study of the steady-state SFD properties. Shown in Figure R11-3-1 is a comparison of the high triangularity standard divertor configuration and the SFD obtained from it. The SFD configuration has a larger region with very low B_p: it extends over most of the outer divertor leg and also penetrates deeper into the pedestal region.

The SFD formation was always followed by a partial detachment of the outer strike point. Despite the detachment high core confinement was maintained with the three-coil SFD. This was evidenced by the factors $\tau_E \leq 50 - 60$ ms, $W_{MHD} \leq 200 - 250$ kJ, and the H98(y,2)~ 1 (estimated using the TRANSP code) similar to those of the standard divertor discharges. Core carbon concentration and radiated power were reduced by up to 30-50 %, apparently as a result of reduced divertor physical and chemical sputtering in the SFD as well as ELMs. During the extended SFD period, medium-to-large size ($\Delta W_{MHD}/W_{MHD} \leq 5 - 12$ %), Type I, ELMs reappered, in contrast to the standard divertor discharges where ELMs were suppressed via the use of evaporated solid lithium coatings on divertor PFCs [R11-3-9].

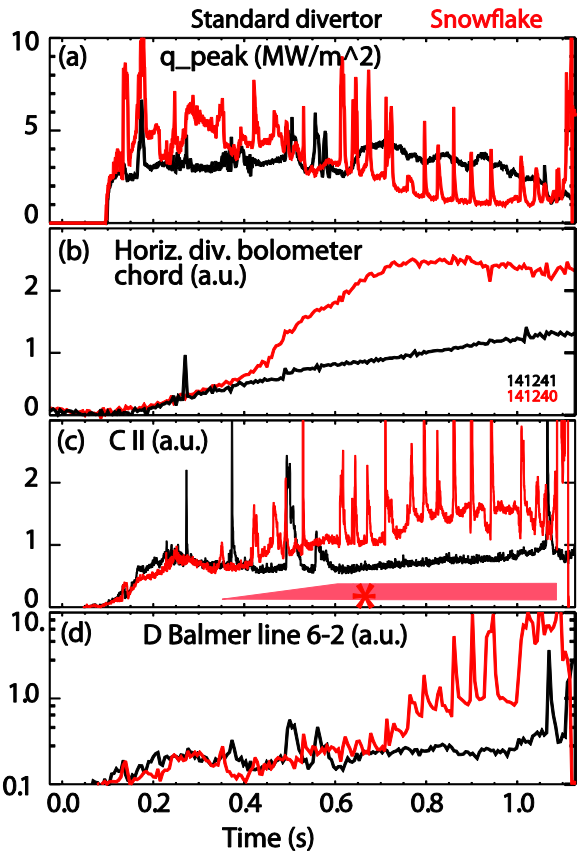

Figure R11-3-2: *Divertor time traces of two similar (standard divertor vs. SFD) discharges: (a) peak heat flux;(b) horizontal bolometer signal; (c) C II brightness;(d) Balmer B6 brightness in the strike point region.*

In the three-coil SFD configurations, a significant reduction of divertor heat flux and increase of carbon radiation were measured. Shown in Fig. R11-3-2 are the time traces contrasting divertor measurements in the SFD and in the standard divertor discharges with the SOL power $PSOL = 2.5 - 3$ MW.

Shown in Fig. R11-3-3 are the lower divertor heat flux, CIII and CIV brightness profiles at the times of interest in the SFD discharge. The lower divertor power (obtained by integrating the heat flux profiles) was $P_{div} = 1.8 - 2$ MW before the SFD, $P_{div} = 1.0 - 1.2$ MW during the SFD formation, and $P_{div} = 0.5{-}0.65$ MW later in the radiative phase of the discharge.

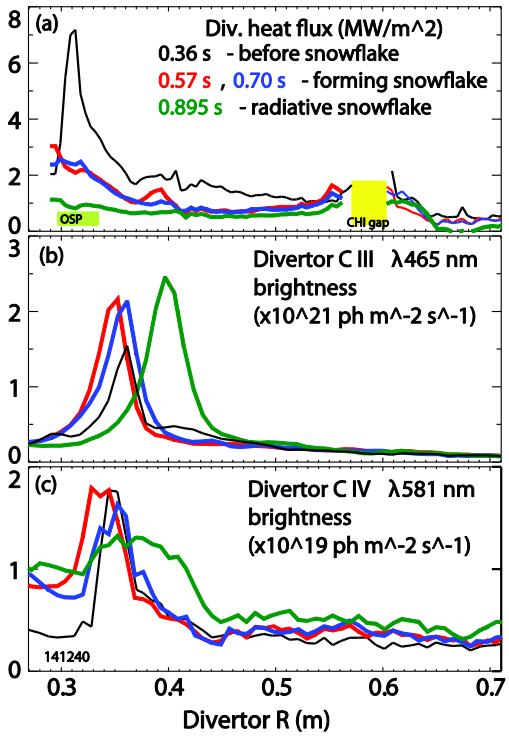

Figure R11-3-3: *Divertor profiles in the SFD discharge at 0.36 s, 0.57 s, 0.70 s and 0.895 s: (a) heat flux; (b) CIII and (c) C IV brightness.*

In NSTX SFD discharges, the radiative detachment was obtained at or shortly after the SFD formation. Based on the present observations, it appears that the partial detachment, when formed, brings additional dissipative losses; however, the SFD alone (even during the formation phase) reduces steady-state heat flux by 50-60% and increases divertor P_{rad} by up to 50%.

Edge transport modeling of the NSTX SFD experiments has commenced using the 2D multi-fluid code UEDGE [R11-3-10]. Shown in Fig. R11-3-4 is a comparison of modeled divertor profiles for the standard divertor and for the snowflake-minus configurations described in detail in Ref. [R11-3-5, 6]. The simulations indicated a tendency for colder, denser plasma in the SFD vs. the standard divertor; however, more work is needed to match the experimental profiles and use the model in the interpretive sense. While the shown profiles did not indicate the partial detachment observed in the experiment, large reductions in T_e and T_i, particle and heat fluxes were seen in the high flux expansion zone of the SFD.

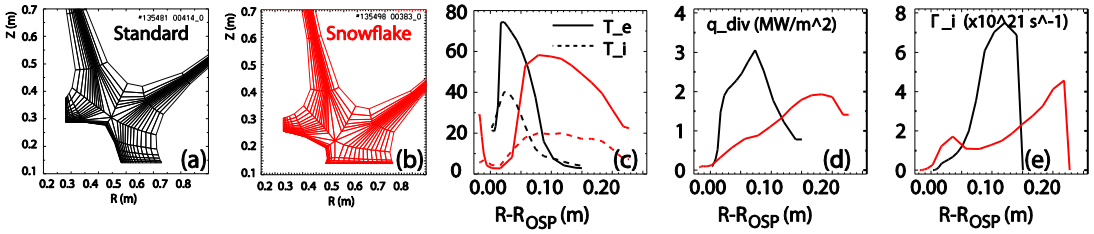

Figure R11-3-4 *- UEDGE model results of the standard divertor (black lines) and SFD (red lines): (a, b) divertor region computation mesh; divertor plate profiles: (c) T_e,T_i, (d) heat flux density; (e) particle flux density.*

As previously reported in FY2010 as part of FES Joint Research Target research, the three U.S. tokamak facilities including NSTX measured a strong inverse dependence of the scrape-off-layer (SOL) heat flux width on plasma current. In NSTX Upgrade plasmas operating the 2MA, the SOL width may narrow substantially potentially challenging the thermal capabilities of the divertor plasma facing components. As a result, operation with a high flux expansion divertor (i.e. the snowflake divertor) may be required to achieve long-pulse NSTX Upgrade plasma full current (2MA) and heating power (10-15MW). In preparation for snowflake control for NSTX Upgrade, a snowflake divertor-tracking algorithm [R11-3-11] was implemented and tested on experimental NSTX data. This algorithm is a one-step algorithm (no iteration is needed) that is fast enough to be used in real-time plasma control system (PCS).

In the algorithm, the snowflake centroid and secondary X-point is located by using the local expansion of the Grad-Shafranov equation in toroidal coordinates:

$$(R+x)\frac{\partial}{\partial x}\left(\frac{1}{R+x}\frac{\partial \Psi}{\partial x}\right)+\frac{\partial^2 \Psi}{\partial z^2}=0$$

Keeping the 3rd order terms and the magnetic nulls is obtained as follows:

$$\Psi_{00} = \Psi_f - \Psi(\rho_f,\zeta_f)$$
$$= \Psi_f - \left[l_2\zeta_f + q_3\zeta_f^2 + c_4\zeta_f^3 + l_1\rho_f + 2q_2\rho_f\zeta_f + (-3c_1 - q_3)\rho_f\zeta_f^2 + \frac{1}{2}(l_1 - 2q_3)\rho_f^2 + (-3c_4 + q_2)\rho_f^2\zeta_f + c_1\rho_f^3 \right]$$

$$\Psi_1 = \Psi(\rho_1,\zeta_1) + \Psi_{00}$$
$$\Psi_2 = \Psi(\rho_2,\zeta_2) + \Psi_{00}$$

The coefficients in the formulation are found from sample points, turning the snowflake tracking into a matrix inversion problem. The algorithm does not need iteration, thus enabling fast tracking in real-time. Figure R11-3-5 shows example tracking results via this algorithm. The results are very robust with convergent results even when the full EFIT reconstruction is not, and the achieved the accuracy is sufficient for control purposes. Since upper and lower snowflake operation may be required in NSTX Upgrade, the PCS software is presently being modified to track and control upper and lower snowflake configurations.

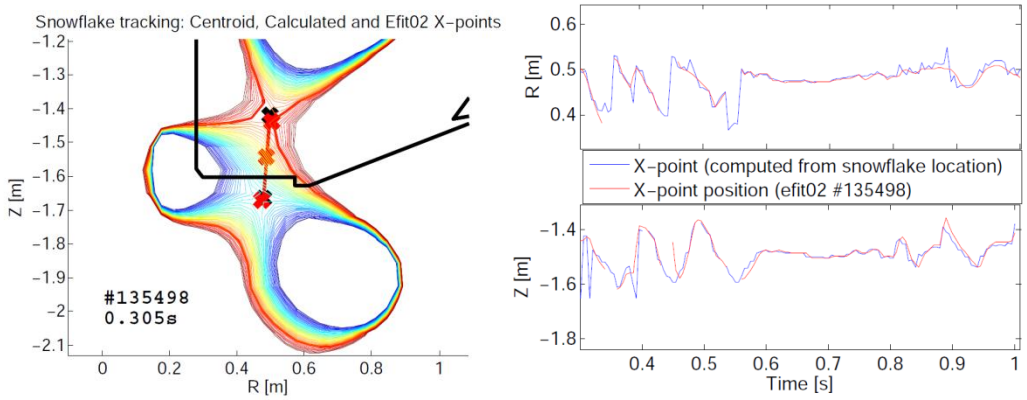

Figure R11-3-5: *Left: Snowflake tracking for NSTX where the red crosses are the snowflake centroid and the X-points calculated via snowflake tracking while the black crosses are the EFIT02 X-points. Right: Comparison of the X-point position computed via snowflake tracking and EFIT02.*

References

[R11-3-1] RYUTOV, D., Phys. Plasmas 14 (2007) 064502.
[R11-3-2] RYUTOV, D. et al., Phys. Plasmas 15 (2008) 092501.
[R11-3-3] RYUTOV, D. et al., *Fusion Energy 2008 (Proc. 22nd Int. Conf. Geneva)* IC/P4-8
[R11-3-4] UMANSKY, M. et al., Nucl. Fusion 49 (2009) 075005.
[R11-3-5] SOUKHANOVSKII, V. A. et al., J. Nucl. Mater., at press (2011).
[R11-3-6] SOUKHANOVSKII, V. et al., Nucl. Fusion 51 (2011) 012001.
[R11-3-7] RYUTOV, D. et al., Plasma Phys. Control. Fusion 52 (2010) 105001.
[R11-3-8] KOLEMEN, E. et al., *Fusion Energy 2010 (Proc. 23nd Int. Conf. Daejon)* EXD/P3-18
[R11-3-9] MAINGI, R. et al., Phys. Rev. Lett. 103 (2009) 075001.
[R11-3-10] ROGNLIEN, T. D. et al., J. Nucl. Mater. 196-198 (1992) 347.
[R11-3-11] MAKOWSKI, M., et al, "X-Point tracking algorithm for the snowflake divertor", personal communication (2011).

FY2011 Research Milestone R(11-4): H-mode pedestal transport, turbulence, and stability response to 3D fields (Target - September 2011. Partially completed – September 2011)

Milestone Description: The use of three-dimensional (3D) magnetic fields is proposed to control the H-mode pedestal to suppress ELMs in ITER. However, the mechanisms for particle and thermal transport modification by 3D fields are not well understood. On NSTX, 3D fields are observed to trigger ELMs in ELM-free discharges and this triggering has been exploited to reduce impurity and radiated power buildup. The mechanisms for this triggering are also not well understood. As observed on other experiments, the plasma response to 3D fields in NSTX is sensitive to the edge q value – in particular, the threshold for triggering ELMs with applied n=3 fields varies non-monotonically with q95. To better understand these findings, this milestone will explore possible mechanisms for modifying particle transport, thermal transport, and the resultant modifications to the pedestal kinetic profiles and ELM stability. Example possible mechanisms include: zonal flow damping, stochastic-field-induced E×B convective transport, and banana diffusion or ripple loss. Pedestal turbulence trends as a function of applied field will be measured with BES, high-k scattering, and gas-puff imaging. Edge particle transport will be measured using improved Thomson scattering, impurity injection, and edge SXR. If available, more flexible 3D field control will be used to vary the applied spectrum. The underlying 3D equilibrium is also a very important determinant of the 3D edge transport, and the transport and turbulence measurements combined with other edge measurements will be utilized to help infer whether the edge plasma response is predominantly ideal or resistive/stochastic in nature. These measurements and comparisons to theory will contribute to improved understanding of the transport and stability response of the pedestal to 3D fields for ITER.

Milestone R(11-4) Report:

ELM destabilization by 3D fields has been observed for several years on NSTX, and in FY2011, an analysis of ELM destabilization experiments using 3D fields was performed using several modeling tools developed for stellarators. Model 3D MHD equilibria were generated with VMEC, which assumes nested flux surfaces and therefore screening of resonant perturbations, and SIESTA, which assumes that current sheets at rational surfaces are dissipated and can treat islands and stochastic regions. These equilibria were used to calculate transport due to stochasticity as well as neoclassical effects, and the resulting transport rates compared to interpretive modeling of the edge transport in experiment using the SOLPS code. With the SIESTA magnetic field, the stochastic transport was calculated to be small compared to experiment (Figure R11-4-1), indicating that the plasma response strongly reduces resonant perturbations. Similarly, neoclassical heat and particle transport is calculated to be much smaller than experiment (Figure R11-4-2), although further calculations suggest that this may be an important transport channel in reduced colllisionality plasmas such as will be obtainable in the NSTX Upgrade. These results are consistent with the lack of temperature flattening observed in the measured pedestal profiles. Ballooning stability was calculated using the COBRA code, and the 3D fields were found to mildly degrade stability. In the future, low-n stability studies will be undertaken, as these are more likely to be relevant to ELMs.

Overall, these results indicate that the 3D neoclassical and stochastic transport of heat and main ions is subdominant to other mechanisms such as 2D neoclassical and turbulent transport in NSTX. These results motivated an investigation of impurity particle transport response to 3D fields as a possible means of improving the understanding of plasma response to 3D fields.

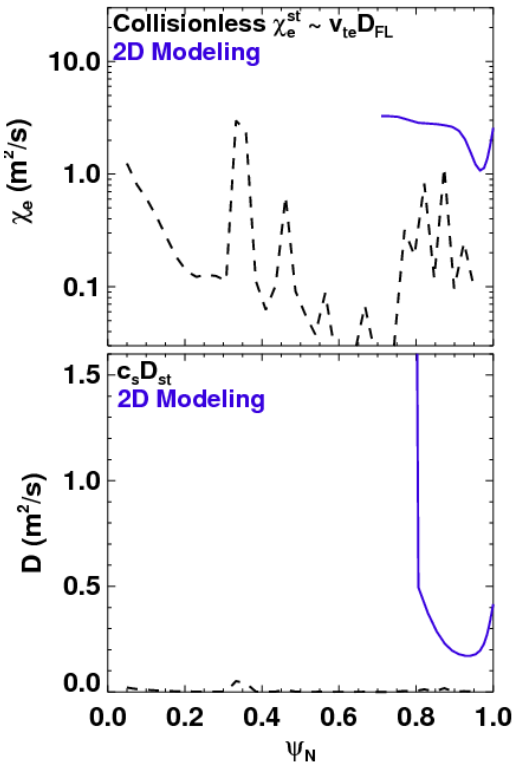

Figure R11-4-1*: Profiles of a) electron thermal and b) particle thermal diffusivity due to stochastic transport using SIESTA magnetic field (solid black/red) and inferred from 2D modeling of experiment (dashed blue)*

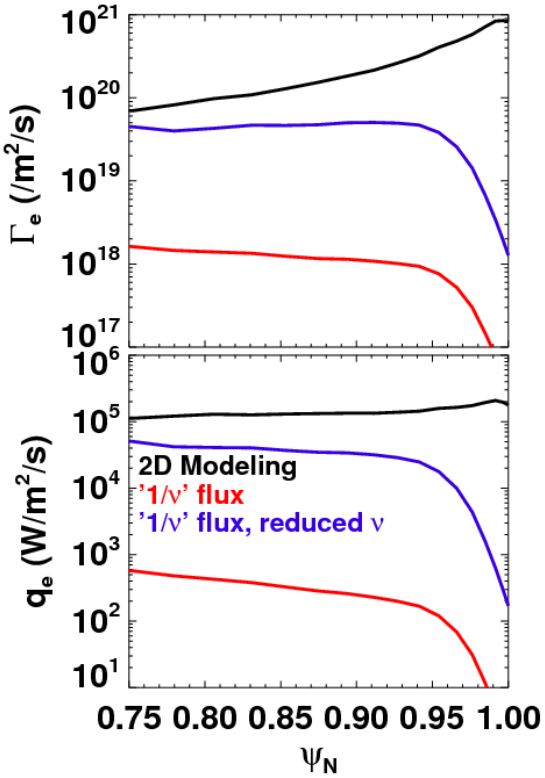

Figure R11-4-2: *Neoclassical and SOLPS profiles a) particle and b) electron heat fluxes.*

In support of improved edge impurity transport measurements, the photodiode-based multi-energy soft x-ray (ME-SXR) diagnostic took first data during the FY11 run campaign. An experiment was conducted in which neon gas injections were used for perturbative impurity transport measurements in the plasma edge. B_T and q scans were performed. Lithium was only applied at the start of the run day, thus as the experiment progressed, ELMs emerged and modified the edge transport and associated measurements. The initial analysis described here focuses on ELM-free discharges in order to test methods of calculating the impurity transport coefficients under conditions which are nearly stationary on a transport time-scale.

The STRAHL 1-D impurity transport code was used to model the diffusion and convection of each impurity charge state, using ionization and recombination rates from the ADAS atomic database. A synthetic diagnostic is then used to calculate the expected ME-SXR signal, using ADAS emission coefficients to calculate x-ray emission from the modeled charge state distribution. A Levenberg-Marquardt chi-square minimization technique is employed to find the diffusion and convective velocity profiles that produce the best fit to the available data. Figure R11-4-3 highlights results from a 1.1 MA, 0.55 T NSTX discharge. Figure R11-4-3(a-b) show the x-ray brightness measured with the 5 μm Be-filtered ME-SXR array following a neon gas puff and the best-fit x-ray brightness from STRAHL. Figure R11-4-3(c) shows the total radiated

power both measured and modeled in the plasma edge. The best fit to the data was produced with the diffusion profile in Fig. R11-4-3(d). This profile is consistent with results from the previous, scintillator-based ME-SXR diagnostic, which measured neon transport inside r/a ~ 0.8 [R11-4-1]. Unfortunately, the TF fault stopped operation of NSTX before experiments utilizing the ME-SXR array could be utilized in experiments studying the effects of 3D fields on impurity transport.

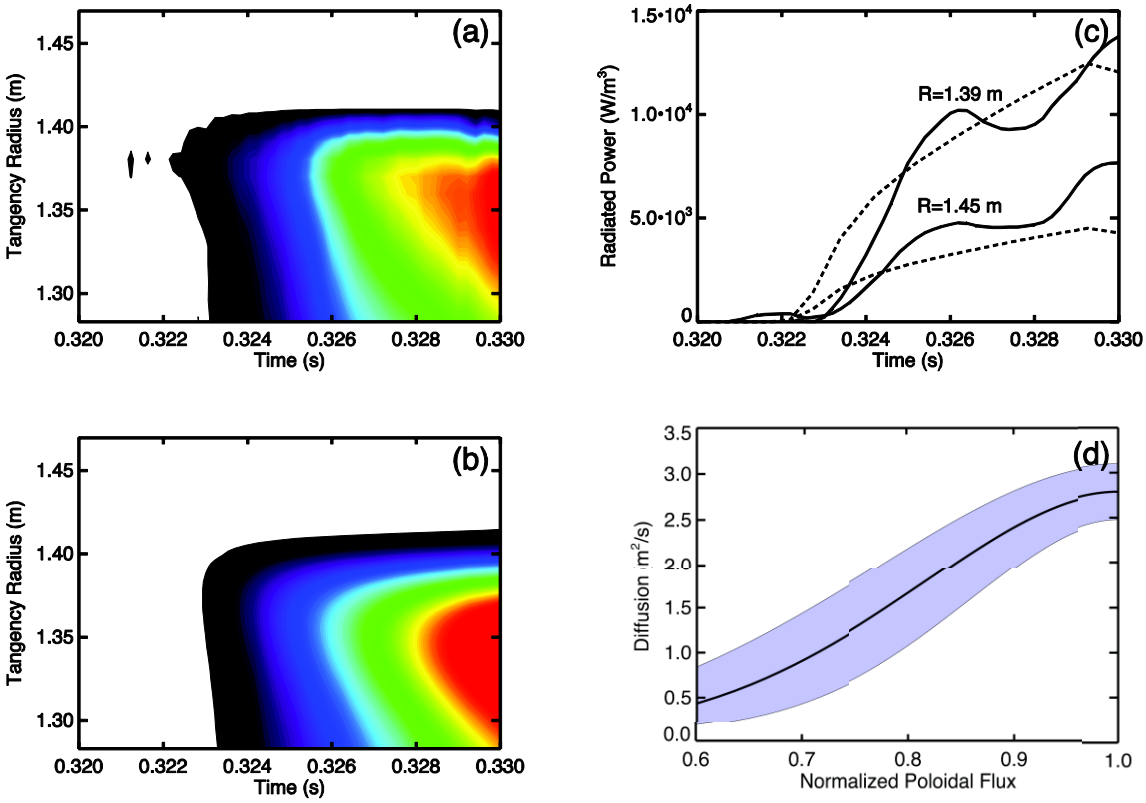

***Figure R11-4-3**: (a) X-ray brightness from injected neon measured with the 5 μm Be ME-SXR array. (b) X-ray brightness from modeling. (c) Total radiated power measured by bolometry (solid line) and computed from best-fit STRAHL run (dashed). (d) Radial diffusion profile that best fits the data, with the shaded region representing the uncertainty. Note that the model is not well constrained towards the core since x-ray emissivity is not measured inside $\Psi_N \sim 0.6$.*

In support of the above experiments, impurity particle transport with 3D fields was also studied theoretically/numerically using IPEC and 3D neoclassical theory to predict the expected experimental measurements planned using on the new ME-SXR diagnostic capability. Based on Non-Ambipolar (NA) transport theory, it has been predicted that impurity transport in the edge scales by $D_{NA,s,1/\nu} \propto M_s^2 T_s^{7/2} I_{3D}^2 N_D^{-1} Z_s^{-4}$, where M_s is the mass, T_s is the temperature, Z_s is the charge of impurity ions, I_{3D} is the current in 3D field coils and N_D is the density of main deuterium ions. The expected scaling is largely different from 2D neoclassical prediction due to 1/ν-dependency in 3D neoclassical transport. Assuming Pfirsh-Schlüter (PS) regime for 2D neoclassical transport, the ratio of the two has been predicted with a scaling $D_{NA,s,1/\nu} / D_{PS,s} \propto M_s^2 T_s^4 I_{3D}^2 N_D^{-2} Z_s^{-4}$. The strong temperature scaling implies that impurity transport enhancement would be measurable for higher temperature, as well as higher mass and larger 3D coil currents. Particle diffusivity calculations using kinetic profiles in previous NSTX

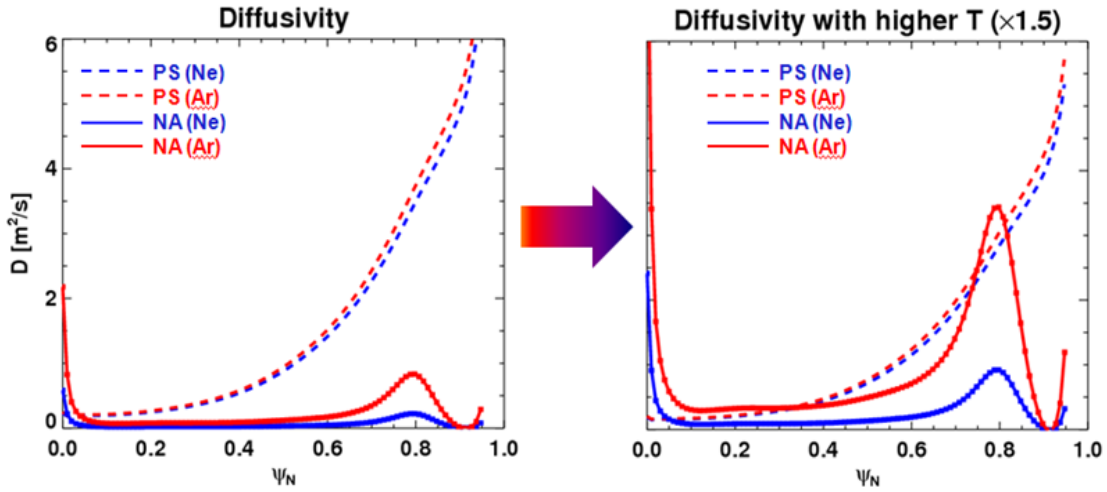

Figure R11-4-4: *Comparison of particle diffusivity profiles predicted by 3D (NA) and 2D (PS) neoclassical theory, for Neon and Argon impurity ions, when n=3 I_{EFC}=2kA is applied. The expected 3D transport is relatively weak for typical NSTX discharges with core T_e~0.8keV, as shown on the left, but can be increased up to a measurable level if Te is increased by a factor of 1.5, as shown on the right.*

discharges, Figure R11-4-4, show that 3D impurity transport (NA) may be dominated by 2D transport (PS), but may be measurable if the temperature is increased by a factor of 1.5.

The above transport analysis and simulations indicate that increased electron and ion temperature achieved through increased plasma current and/or operation in the NSTX 'enhanced pedestal' H-mode [R11-4-2] could enable access to edge plasma conditions where 3D neoclassical particle transport rates are compare to 2D neoclassical transport and could be measured and utilized to understand plasma response to 3D fields. More importantly, increased temperature and reduced collisionality should be readily accessible in NSTX Upgrade due to increase toroidal field, plasma current, and heating power. Thus, perturbative impurity transport experiments to better understand the transport response to 3D fields should be readily achievable in NSTX Upgrade.

References

[R11-4-1] L. Delgado-Aparicio et al., Nucl. Fusion 51, 083047 (2011)

[R11-4-2] R. Maingi, et al., Phys. Rev. Lett. 105, 135004 (2010)

Additional NSTX Research Achievements in FY2011:

Beyond the progress toward and/or completion of the FY2011 research described above, several additional important scientific and operational results were obtained during the FY2011 run and are described below.

Solenoid Free Plasma Start-up (SFPS) Research for NSTX and NSTX Upgrade

The SFPS program had three experimental run days during FY2011 run and these run days contributed to a significantly improved understanding of CHI in three specific areas:

1. Demonstration of further savings of central solenoid flux
2. Evidence for the generation of near 400kA of peak CHI start-up current
3. Further analysis of these data suggested very high current start-up capability in NSTX-U

In addition, considerable progress was made in CHI discharge simulation capability:

4. Simulations with the TSC code were able to show consistency with previous theoretical scaling of CHI and showed high start-up current projections as both the injector flux and toroidal field are increased.
5. First use of the NIMROD code for simulating CHI discharges in NSTX.

Results from these five activities are briefly summarized below.

Experimental Results

CHI is implemented in NSTX by driving current along field lines that connect the inner and outer lower divertor plates. The standard operating condition for CHI in NSTX uses the inner vessel and lower inner divertor plates as the cathode while the outer divertor plates and vessel are the anode. A CHI discharge is initiated by first energizing the toroidal field coils and the lower divertor coils to produce magnetic flux linking the lower inner and outer divertor plates which are electrically isolated by a toroidal insulator in the vacuum vessel. After a programmed amount of gas is injected into the vacuum chamber, a voltage is applied between these plates which ionizes the gas and produces current flowing along magnetic field lines connecting the plates. In NSTX, a 5 to 30 mF capacitor bank charged to 1.7 kV provides this current, called the injector current. As a result of the applied toroidal field, the field lines joining the electrodes wrap around the major axis many times so the injector current flowing in the plasma develops a much larger toroidal component.

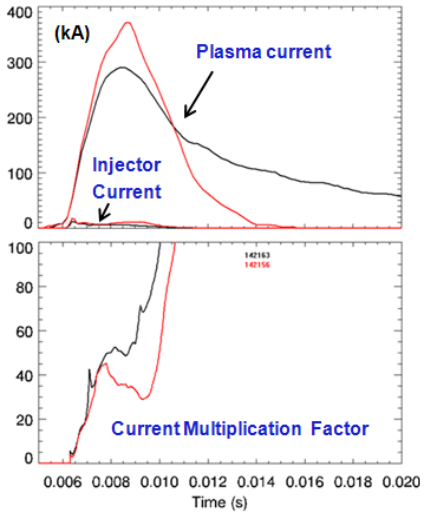

Figure CHI-1: *A CHI-only started discharge (142156) that reached nearly 400kA but decayed faster than the 300kA discharge because it developed an absorber arc. Also shown is the current multiplication factor for both discharges.*

During FY11, in CHI-only discharges, start-up currents approaching 400kA were generated (Fig. CHI-1), but developed absorber arcs and so had rapid current decay rates. Additional discharge optimization to avoid absorber arcs and further increase the plasma current in these high current CHI-initiated plasmas was planned for NSTX and will be carried out in NSTX Upgrade.

The results reported here were made possible by reductions to the low-Z impurities, mainly oxygen and carbon, as previously reported. Fig. CHI-2 shows a recent (FY11) CHI started discharge that was coupled to induction. The second discharge is an inductive-only case from the NSTX database (assembled over 10 years of operation) that reached 1 MA in a shorter time than other L-mode discharges. For the CHI initiated discharge at 132 ms, a total of 258 mWb of central solenoid flux was required to ramp the discharge to 1 MA. The non-CHI discharge at this time only gets to about 0.7 MA and does not reach 1 MA until 160 ms, by which time 396 mWb of central solenoid flux had been consumed. Thus, the L-mode discharges from the NSTX data base require at least 50% more inductive flux than discharges assisted by CHI. The discharge on NSTX that consumed the least amount of solenoid flux to reach 1 MA transitioned to an H-mode. That discharge required 340 mWb to reach 1 MA, which is still significantly higher than the CHI started discharges.

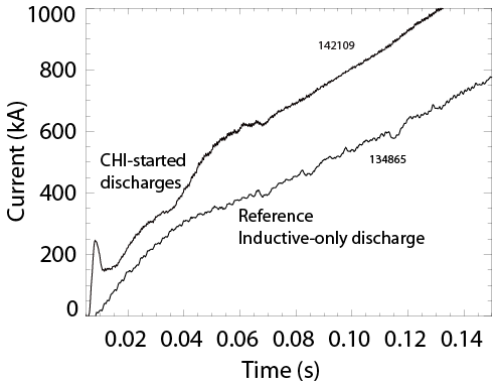

Figure CHI-2: *Shown are a CHI started discharge and a reference inductive-only discharge.*

These new discharges continue to exhibit favorable properties described in the FY10 annual report, adding confidence to the robustness of the quality of CHI started discharges in NSTX. These favorable properties are likely the result of the hollow electron temperature profile and rapid inductive ramp, the resultant very low internal inductance $l_i \approx 0.3$ and very high elongation of $\kappa \approx 2.6$, all from the beginning of the discharge. Finally, these plasmas are relatively free of MHD activity despite having low density, which has previously been associated with increased instability during normal inductive startup.

Projections to NSTX-U

Analysis of results from NSTX shows that CHI has the potential for generating significantly increased start-up plasma current in NSTX Upgrade due to improved injector coil design and higher toroidal field capability of 1T, consistent with earlier theoretical calculations and more recent TSC simulations that are described below. The results from the analysis of experimental data are summarized in Table CHI-1.

Parameters	**NSTX**	**NSTX-U**
R (m)	0.86	0.93
a (m)	0.68	0.62
B_0 (T)	0.55	1.0
Toroidal flux (Wb)	2.68	3.78
Normalized internal inductance, l_i	0.35	0.35
Planned non-inductive sustainment current I_{ps} (MA)	0.7	1.0
Poloidal flux at I_{ps} (mWb)	132	206
Maximum available injector flux (mWb)	80	340
Max. startup current potential (MA)	0.4	~1
Required injector current for max. current potential (kA)	10	27*

Table CHI-1: CHI startup parameters in NSTX and NSTX-U
*HIT-II routinely operated with 30kA injector current without impurity issues

Table CHI-1 shows that at a normalized internal inductance of 0.35, obtained in NSTX, a 1MA NSTX-U discharge with this inductance should have a poloidal flux of 206 mWb. In the absence of poloidal flux amplification, the amount of toroidal current a CHI-started discharge can generate is directly proportional to the amount of poloidal flux injected. NSTX-U has the potential for injecting up to 340 mWb of poloidal flux, compared to just 80 mWb in NSTX. NSTX experiments thus far have injected on the order of 50 mWb of flux. This improved current generation potential in NSTX-U is due to the much improved design of the CHI injector flux coil, which is positioned much closer to the CHI insulating gap allowing much more of the flux generated by this coil to usefully connect the inner and outer divertor plates.

Although the injector flux capability in NSTX-U is large, the amount of useful injector flux defined as the amount of flux that can be injected with acceptable amount of low-Z impurities may be determined by electrode conditions and injector voltage limits. This is because a larger value of injector flux requires a higher level of injector current and this may increase the amount of impurity influx. Present NSTX experiments that have a graphite inner divertor electrode have been able to achieve injector current as large as 10 kA and these discharges when coupled to induction have successfully ramped to 1 MA. So this could be assumed to be a lower injector current bound on NSTX-U. Because the toroidal field on NSTX-U is nearly twice that in NSTX, the same value of injector current can inject nearly twice the injector flux in NSTX-U. This should result in a lower bound on CHI produced toroidal current in NSTX-U on the order of 0.5 MA. If the injector current can be increased without creating additional impurity influx, toroidal currents up to 1 MA are projected to be possible in NSTX-U.

TSC Simulations

TSC is a time-dependent, free-boundary, predictive equilibrium and transport code (S. Jardin, PPPL) and has proved to be very useful for modeling CHI discharges and projecting CHI capability in future devices. TSC has been able to show consistency with earlier theory for the scaling of CHI produced current with the injector and toroidal fluxes.

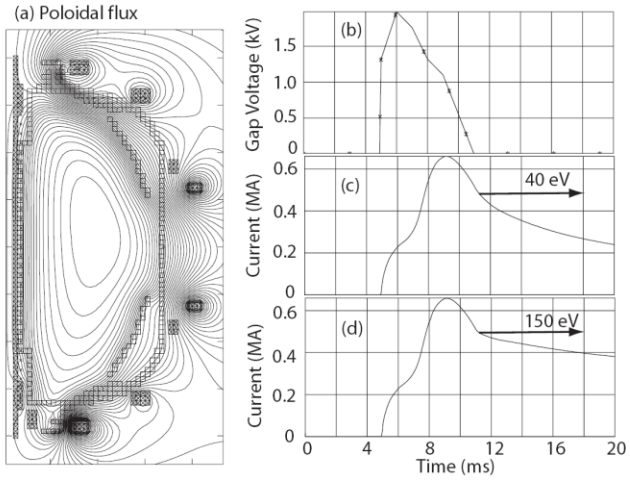

Figure CHI-3: *A TSC simulation with the toroidal field increased to 1 T and the injector flux increased to about 80% of that allowed by the divertor coil current limits in NSTX. Peak toroidal current of 625 kA is generated. The electron temperature throughout the plasma is held at 40 eV and Z_{eff} is 2.5. Shown are (a) the poloidal flux contours at 13.5 ms, (b) the CHI gap voltage, (c) the CHI produced toroidal current and (d) the CHI produced toroidal current for the case in which the electron temperature is increased to 150 eV for times 12 ms and beyond.*

In a simulation run at 1 T toroidal field, it is seen in Fig. CHI-3 that toroidal currents in excess of 600 kA could be achievable in NSTX. The need for the higher toroidal field is to reduce the injector current as this places a limit on the useful poloidal flux that could be injected. Doubling the toroidal field allows the same amount of poloidal flux to be injected at half the injector current.

The applied voltage time history and the attained current are shown in Fig. CHI-3b and c. For the discharge shown in Fig. CHI-3a, the electron temperature was restricted to 40 eV throughout the discharge. If during the current decay phase, starting at about 12 ms, the electron temperature is increased to 150 eV, as might be expected from additional heating sources such as from High Harmonic Fast Wave heating supplemented with early neutral beam injection, then the current decay rate substantially slows down as one would expect. This result is shown Fig. CHI-3d.

NIMROD Simulations

The near-term goals of this research are to use whole device modeling with the NIMROD resistive-MHD code to develop a fuller physics understanding of Coaxial Helicity Injection (CHI) on NSTX, interpret experimental results and support improvement of the process for developing a start-up plasma. The CHI model is a generalization of the one used for injection into HIT-II. Results are compared with NSTX experimental discharges as shown in Figure CHI-4.

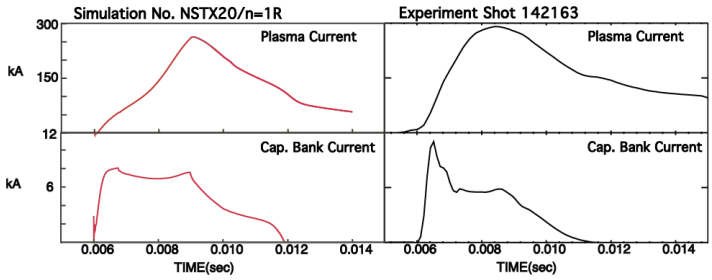

Figure CHI-4: *Comparison of NIMROD computed injector current and plasma current (left) with experimentally measured data (right)*

FY2011 NIMROD modeling accomplishments in include:

- Grids for the NSTX geometry were developed with vacuum magnetic fields calculated either from the poloidal-field coils or from boundary conditions that include wall eddy currents.
- The model used in simulations of HIT-II has been generalized. Voltage across the injection gap is determined by a model of the NSTX CHI power supply; other models can be easily used. Current is measured at the gap and determines the evolution of the capacitor charges and voltages. The voltage across the absorber gap is determined by the ExB outflow balancing vacuum toroidal flux inflow at the injector.
- Ohmic heating and thermal conductivity (along open field lines) are included.
- The expansion of a poloidal-flux "bubble" from the injector is observed and agrees with visual observations on the experiment. Discharge currents and current amplification (toroidal current/discharge current) are in semi-quantitative agreement with experiment (and analytical models) as seen in Fig. CHI-1 which compares a simulation with NSTX shot 142163. Calculated temperatures are in approximate agreement with experiment.
- Simulations show an n=1 mode: an instability in the current channel with poloidal wavelength 0.1-0.3 m results in an helical structure in the current layer at the surface of the expanding flux bubble. The mode can be strong during the early stages of injection, but is less important as the plasma fills the NSTX volume.

Lithium Research

Liquid Lithium Divertor

During the four weeks of experimental operation in FY2011, NSTX continued the use of the Liquid Lithium Divertor (LLD) installed in 2010 on the outer part of the lower divertor. This system was designed to test the effectiveness of a liquid lithium surface refreshed by lithium evaporation in maintaining the deuterium retention properties of lithium. The molybdenum coating on the plasma-facing surface of the LLD has 45% porosity with a capacity to absorb about 40 g of lithium, and to retain it by surface tension against electromagnetic forces. The two NSTX lithium evaporators (LITERs) were used to deposit lithium on the LLD surface. At the beginning of discharges, the LLD lithium surface ranged from solid to liquefied depending on the amount of applied and plasma heating. For the 2011 experiments, hot air was pumped through the heating/cooling tubes of the four plates of the LLD to raise their initial temperatures to 102°C. Subsequent heating of the LLD by the power flowing the plasma divertor scrape-off layer resulted in front-face temperatures reaching 300°C during the plasma pulse, *i.e.*, well above the lithium melting temperature of 180°C. Improvements in plasma performance were obtained similar to those obtained previously with lithiated graphite, *e.g.*, ELM-free, edge-quiescent, H-modes. During these experiments with the plasma outer strike point on the LLD, the amount of deuterium retention in the LLD, as indicated by the fueling needed to achieve and maintain stable plasma conditions, was about the same as that for solid lithium coatings on the graphite prior to the installation of the LLD (Figure LLD-1)., *i.e.*, about twice that of no-lithium conditions.

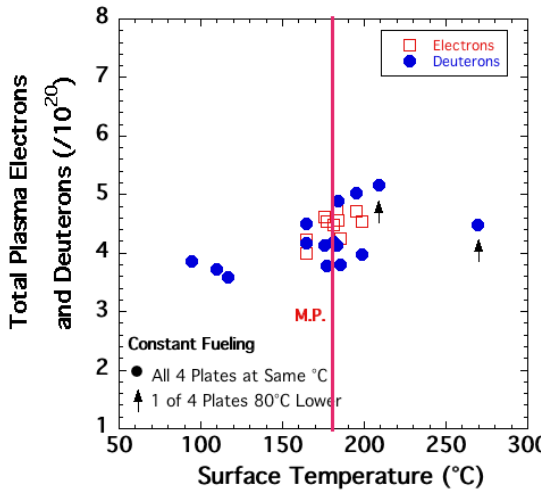

Figure LLD-1: *Total plasma electron and deuterons measured using Charge Exchange Recombination Spectroscopy (CHERS) and the volume average plasma electron content versus LLD surface temperature during the plasma.*

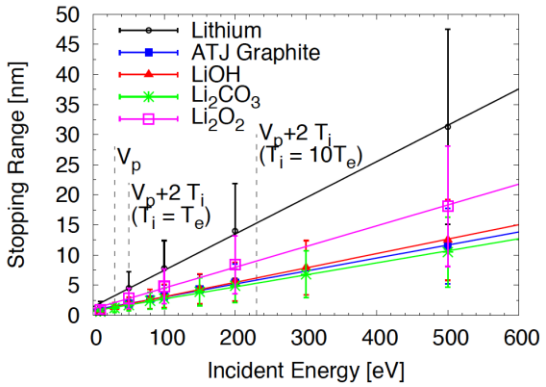

Figure LLD-2: *A calculation with the TRIM code indicates a stopping range of about 5 nm in lithium for 50 eV deuterium ions, and a stopping range of about 3 nm in typical lithium compounds formed with common residual gases in the vacuum environment. Vp is the typical floating potential of a Langmuir probe at the divertor strike point and Ti the typical ion temperature in the plasma scrape-off. In this reference calculation, the ion temperature is assumed equal to the electron temperature, and the incident ion energy is taken as the sum of the measured plasma potential (Vp) and an assumed ion temperature contribution to the incident energy of 2*Ti. Shown also is a deuterium ion energy estimate based on Kocan's report that Ti in various fusion devices could range from 1*Te - 10*Te in the SOL (for all measurements well above the divertor).*

The role of impurities in the lithium surface layers in this result is under investigation. Measurements with the divertor Langmuir probes and the midplane charge-exchange recombination spectroscopy (CHERS) indicate that the energies of diverted deuterium incident on the LLD was about 50 eV. A deuterium stopping range calculation using the TRIM code (Figure LLD-2) indicates that surface layers contaminated by lithium oxidation products with thicknesses of only 3 nm would be sufficient to prevent the incident D ions from reaching the active lithium. Such impurity complexes have been found in laboratory studies on solid lithium deposited on graphite. Laboratory work is in progress to investigate the nature of D-Li-O-C impurity complexes on lithiated graphite and static liquid lithium surfaces, and to characterize their deuterium retention properties.

Plasma response to lithium coatings of plasma facing components

In FY2011, NSTX researchers performed new analysis for a controlled sequence of progressively increasing lithium coatings, discovering that a number of discharge characteristics improved *continuously* with increasing coatings, all with nominal thickness >> the ion implantation depth in the divertor, which is < 10 nm. Li was introduced methodically into an ELMy H-mode discharge scenario with small Type I ELMs. The deposition rate was kept roughly constant between the first 9 discharges, and was gradually increased afterwards.

Results indicate that many plasma parameters changed nearly continuously with increasing lithium coatings [Li-1]. It was found that the divertor recycling light was gradually reduced with increasing lithium wall coatings, and the plasma stored energy and normalized τ_E all increased, while the core T_e and P_e profiles became less peaked with increasing lithium wall coatings. Core transport analysis with TRANSP showed a substantial drop in edge electron transport. Figure Li-1(a) shows that both the total and electron τ_E increased with increasing lithium deposition; indeed, the electron τ_E increased more rapidly than the global τ_E. Figure Li-1(b) shows the core electron and ion thermal diffusivities, χ_e and χ_i at r/a=0.35 were insensitive to or weakly increasing with the pre-discharge lithium deposition. In contrast, the edge χ_e at r/a=0.7 decreased strongly with increasing lithium deposition (Figure Li-1(c)); however, the ion thermal diffusivity χ_i actually increased modestly. These results indicate that the changes in the edge electron transport dominate, since the total τ_E was also increasing.

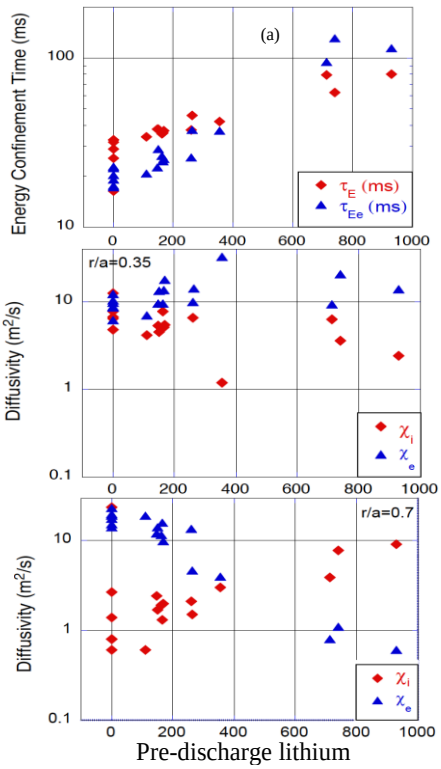

Figure Li-1: *Results of core transport analysis as a function of pre-discharge lithium evaporation (in milligrams) for discharges with I_P = 0.8MA B_T = 0.45T, P_{NBI} = 4MW, and line average n_e from 4 - 6.5 x 10^{19} m^{-3}: (a) total and electron τ_E, (b) cross field diffusivities χ_i, and χ_e at r/a = 0.35, and (c) χ_i, and χ_e at r/a = 0.7. The three discharges with highest evaporation had P_{NBI} from 2-3 MW.*

Interpretive 2-D simulations showed [Li-2] that the near-separatrix D_e^{eff} and χ_e^{eff} were reduced substantially from $0.8<\psi_N<0.94$, i.e. the H-mode pedestal effectively expanded to the inner boundary of the calculation in the ELM-free discharge with lithium. The most dramatic changes to the profiles were in the pedestal region, where the n_e and P_e profile widths doubled. Interestingly, the edge T_e gradient remained approximately constant in the H-mode barrier region, but increased just inside the top of the pedestal with increasing wall coatings. The ion pressure profile was changed only modestly; hence, the total pressure profile reflected the modification of the electron pressure profile, whose peak gradient and associated bootstrap current moved farther from the separatrix. These profile changes were clearly correlated with the observed gradual suppression of ELMs with increasing lithium, with reduced drive for the kink/peeling mode being the key stabilizing mechanism.

The ELM frequency during the scan depended on the amount of pre-discharge lithium deposition. Figure Li-2(a) shows that the measured ELM frequency during discharges from this sequence decreased with increasing discharge number, i.e. increasing lithium. The transition to ELM-free operation was not quite monotonic, however, in that several discharges with substantial ELM-free periods were followed by ELMy discharges [Li-3]. The data points in black had edge profiles that were analyzed with an ELM-synchronization method, whereas the data points in blue were unsuitable to create ELM-synced composite profiles, but were included for more insight into the trends. The discharges with more than one data point had both an ELMy and an ELM-free phase.

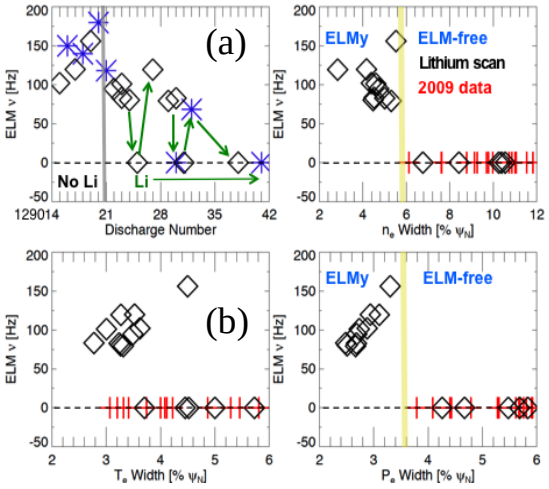

Figure Li-2: *(a) Average ELM frequency during the scan; discharges with both ELMy and ELM-free periods of duration > 100ms are shown with multiple data points. (b) ELM frequency dependence on the fitted widths of the (b) n_e, (c) T_e, and (d) P_e profiles. Converged tanhh fits could not be obtained for the blue data points in panel (a), but are included to reflect the ELM frequency trend.*

The n_e, T_e, and P_e composite profiles were fitted with a 'standard' modified hyperbolic tangent ("mtanh") function, which includes both a tanh and a linear component. The ELM frequency from the black data points is shown as a function of these pedestal widths in Figures Li-2(b-d). The additional data points in red were obtained in discharges with heavy Li wall coatings from the 2009 campaign, using the same discharge programming and reduced P_{NBI}, as in shot 129038. Clearly the ELMy and ELM-free data are separated in the n_e and P_e profile widths, with an apparent threshold for suppression. The T_e profile width can be immediately ruled out as an ordering parameter. Since the Li mainly changes the recycling and the edge fueling, these trends support the hypothesis that the density profile change is central to the ELM suppression.

References

[Li-1] R. Maingi, et al., Phys. Rev. Lett. (2011) – accepted for publication
[Li-2] J. Canik, et al., Phys. Plasmas **18**, 056118 (2011)
[Li-3] D. Boyle, et al., Plasma Phys. Contr. Fusion – submitted 2011

Boundary Physics Research

Edge Turbulence

The formation of the edge transport barrier (ETB) and its correlation with turbulence suppression were investigated in NSTX using the newly implemented ultrafast-swept FMCW reflectometers for n_e profile, k_r backscattering, and radial correlation lengths measurements. Figure BP-1 shows k_r spectra and correlation lengths across the edge region, before and after an Ohmic L-H transition. Locally at the ETB location, turbulence across the entire k_r spectrum is suppressed and the correlation length decreases. This is coupled to an increase in the local electron density gradient, demonstrating a clear connection between the transport barrier formation and turbulence suppression. Oscillatory behavior is often seen leading up to the transition (possible predator-prey behavior); the connection with mean and oscillatory flows is being investigated. This diagnostic is expected to be very useful for improving the understanding of edge turbulence, flows, and edge transport barrier formation in NSTX Upgrade plasmas.

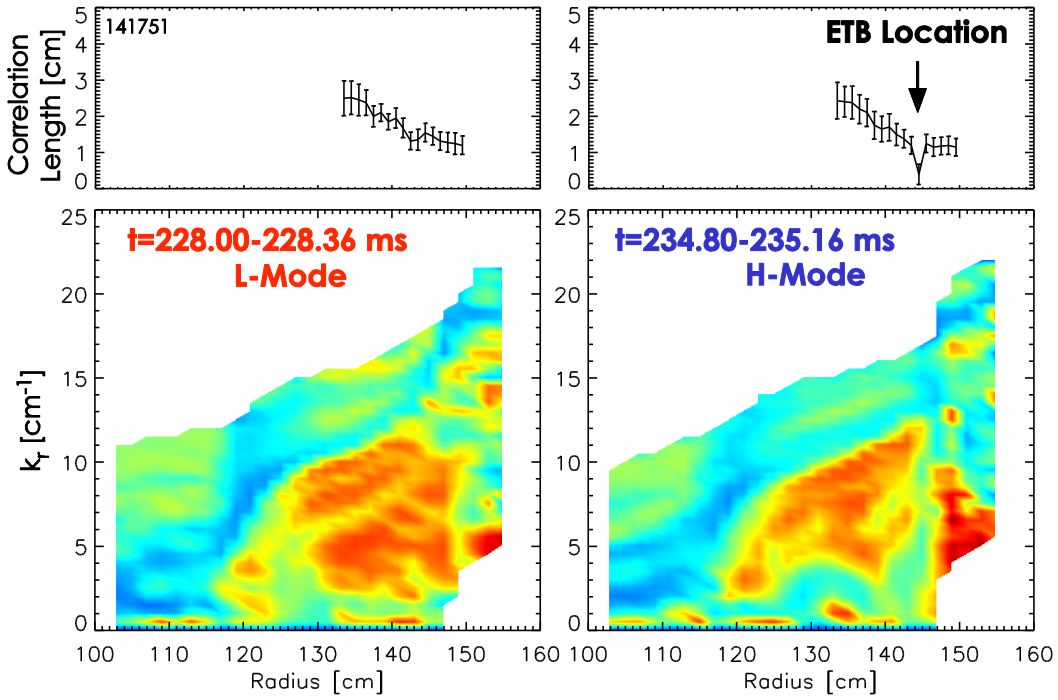

Figure BP-1: *Radial correlation lengths (top) and k_r spectra (bottom), before and after the L-H transition.*

Also in the research area of edge turbulence, analysis continued in 2011 of the oscillating edge zonal-like flow seen in the gas puff imaging (GPI) diagnostic data taken in 2009-2010. These flows were correlated with quiet periods in the edge turbulence preceding the L-H transition [BP-1, 2]; similar oscillations have now been seen on ASDEX Upgrade and DIII-D, suggesting a common phenomenon. New analysis in 2011 showed that in some cases these zonal flow spectra are broadband and intermittent, rather than near-coherent at ~3 kHz. A separate analysis of the statistics of SOL turbulence in H-mode plasmas showed a higher level of blobs/intermittency at longer times after the transition and at higher beam power [BP-3]. An analysis of the H-L back transition in RF heated plasmas shows a very distinct wave-like edge intensity fluctuation with a

20-30 kHz frequency at poloidal wavenumbers between 0.1 and 0.2 cm^{-1}. These fluctuations may be related to the linear instability which generates L-mode turbulence or ELMs.

Two papers were published in 2011 which directly compared NSTX GPI data on edge turbulence with results from the Lodestar scrape-off layer turbulence code SOLT [BP-4, 5]. In [BP-4], various properties of the SOL turbulence as measured by GPI in NSTX in L-mode plasma were directly compared to synthetic GPI diagnostic output from SOLT simulations. Reasonable agreement was obtained, for example, for the number and size of blobs and radial profile of the skewness of the GPI intensity fluctuations (see Figure BP-2). In [BP-5], a new cross-field transport mechanism was discovered in SOLT simulations which dominated the near-SOL heat flux width for NSTX H-modes; namely 'intermittent separatrix-spanning convective cells', in which blob emission in inhibited by shear near the separatrix. A qualitative connection to the experimental GPI data was described in this paper.

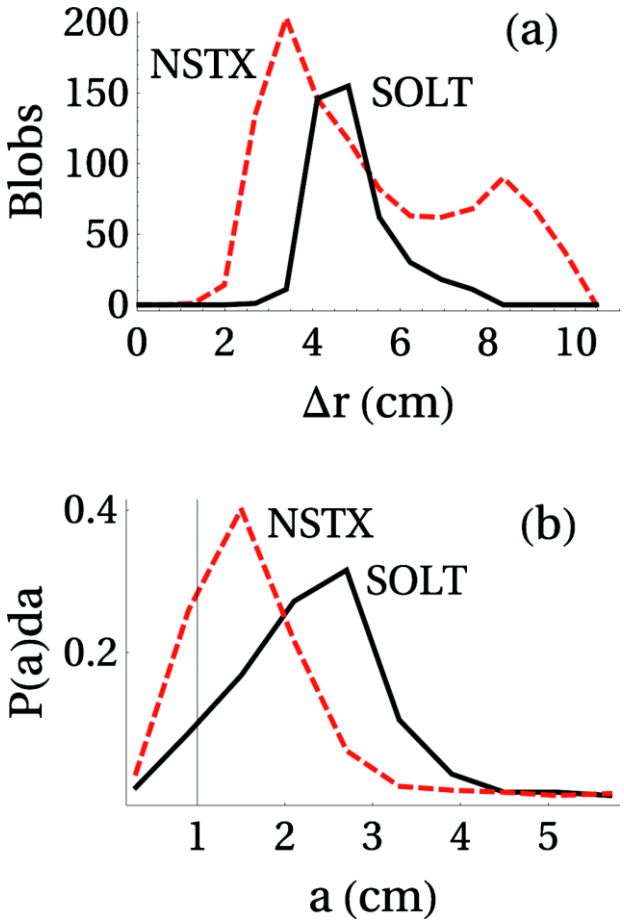

Figure BP-2: *For GPI images in the SOLT simulation (β=1.75× β_0, black, solid) and in NSTX shot no. 112825 (red, dashed): (a) the number of intensity blobs detected vs radius and (b) the distribution of intensity-blob poloidal half-widths. All pdfs use ten uniform bins.*

Divertor Langmuir Probes and Active Divertor Biasing

The High Density Langmuir Probe Array (HDLPA) implemented in the 2010 campaign is yielding significant data for understanding the divertor plasmas in NSTX as well as plasma-wall interactions. In addition to the Lithium Research and Boundary Physics TSGs, the Waves and Energetic Particles TSG has found the probe data useful in FY2011 for analysis and interpretation of the hot-spots observed on the divertor floor during RF heating. Specific challenges, however, face the usage of Langmuir probe data during typical operation of the NSTX device. These include appropriate determination of relative probe position with respect to the strike point and the specific choice of probe interpretation methodology. With the inclusion of magnetics data and equilibrium reconstructions, it is possible to determine the structure of the scrape-off layer as the strike-point oscillates during the discharges.

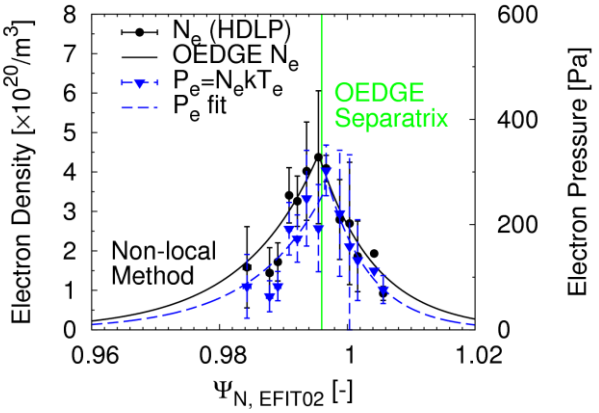

Figure BP-3: *Electron density and pressure vs. normalized poloidal flux as measured by the high-density Langmuir probe array in the lower divertor of NSTX.*

Interpretation of the swept Langmuir probes I-V characteristics has been carried out by two methods: classical interpretation and non-local interpretations. The "classical" method utilizes a Boltzmann fluid assumption for the I-V characteristic up to the floating potential, but not beyond. The non-local method, demonstrated most recently on CASTOR tokamak, is capable of interpreting the entire I-V characteristic provided the probe is operating in the appropriate regime. The I-V characteristic analyzed by the non-local method is able to infer the electron energy distribution function of the plasma.

It has been found that in a typical medium triangularity discharge shape, that the NSTX outboard divertor is dense (2-5x10^{20} m^{-3}) and cool (~5eV). Profiles are shown in Figure BP-3. Further, the EEDFs indicate that the classical method is entirely determined by a hot tail population yielding anomalously high temperatures if one assumes a Maxwellian distribution based on this interpretation method. An example EEDF is shown in Figure BP-4. Preliminary spectroscopic analysis indicates a density in the strike-point

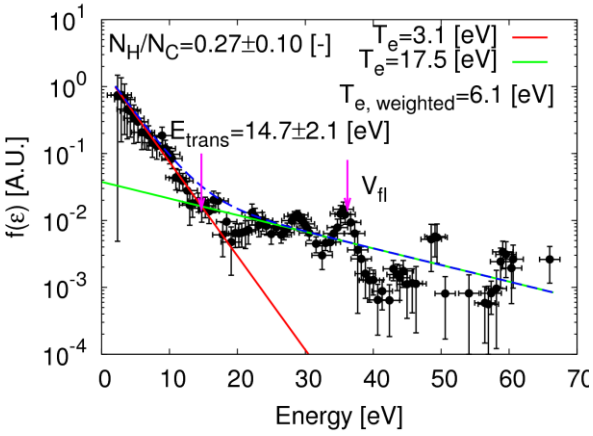

Figure BP-4: *Electron Energy Distribution Function (EEDF) measured with the high density divertor Lanmuir probe array.*

region of 3-5x10^{20} m^{-3} via line broadening methods – corroborating the non-local interpretation of the Langmuir probes. The Classical interpretation would yield a density approximately half the value of the non-local method, which is too low in density to correspond with the spectroscopic signal. Further, the existence of high-N Balmer lines (N=10) implies low temperatures, similar to the 2-5eV measured. These results corroborate the probe interpretation.

Further interpretation of the NSTX diagnostic set in the divertor is being performed with the aid of the OEDGE interpretative code suite. This set utilizes Onion-Skin Method (OSM) modeling to reconstruct the background plasma based on the divertor target conditions. Estimates taking into account the non-Maxwellian distribution of electrons are being made for the incident heat flux determining the effective sheath heat transmission coefficient of the plasma. These estimates compare favorably with the measured fluxes. Contributions from neutrals and radiation are being included and constraining in the plasma modeling to determine the degree of consistency between diagnostics using the OEDGE framework.

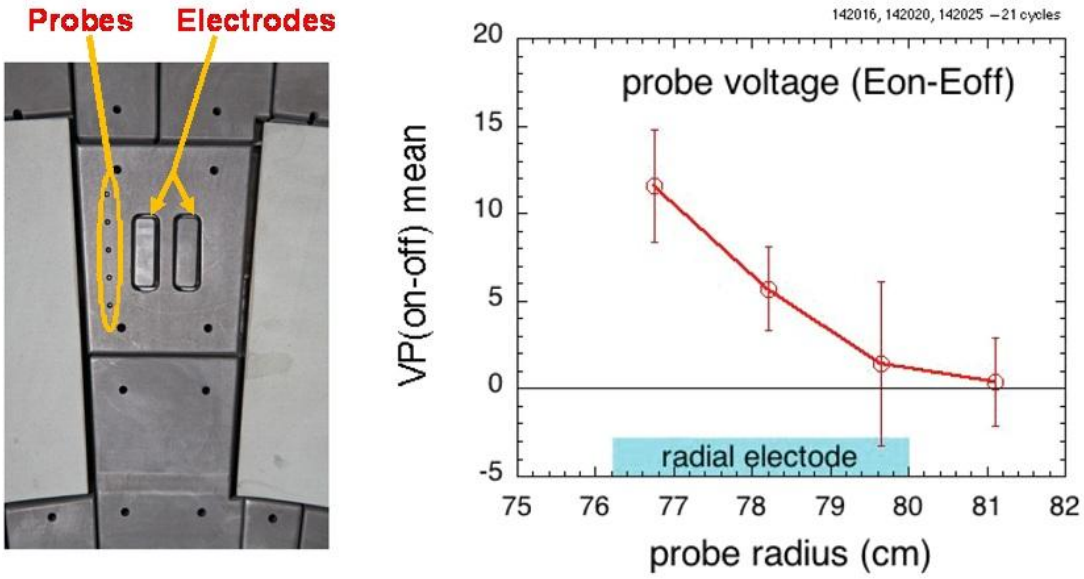

Figure BP-5: *(Left) photo of the biased divertor electrodes and nearby probes (these probes are not part of the HDLPA). (Right) change in probe floating potential with +50 Volt biasing on the radial electrodes. There is a radial asymmetry which may be due to the convective cell flow direction.*

Beyond measurements of the plasma characteristics in the divertor region, experiments have also been performed (data obtained in 2010) to test a theoretical proposal to control the plasma flux to a tokamak divertor plate by creating local convective cells using electrostatic biasing [BP-6]. This convective cell motion can in principle increase the radial cross-field transport significantly and thus spread the heat flux over a wider area at the divertor plates. The experiments on NSTX were done using two pairs of small electrodes (4 cm x 1.5 cm) embedded in diagnostic tiles in the lower divertor, along with a set of 5 Langmuir probes in a radial array near each pair of electrodes. One pair of electrodes was oriented radially (see left photo of Figure BP-5), and the other pair was elongated toroidally, and the electrodes could be biased at up to ±90 VDC.

Analysis performed in FY2011 indicates that the clearest results from biasing came during experiments in which the outer divertor strike-point was near the major radius of these electrodes and the electrode current was highest (~30 Amps/electrode at +50 Volts bias). As shown in Figure BP-5, for the electrodes oriented radially, biasing caused some of the nearby probe's floating potentials to increase by ≥ 10 volts and their ion saturation currents to increase by a factor ≥ 5, similar to previous results at the outer midplane of NSTX [BP-7]. This shows that divertor electrode biasing can affect the local SOL plasma as suggested by the theory. Interestingly, under similar conditions much less effect was seen for the electrodes oriented toroidally. The extent of these perturbations along and across B is being analyzed experimentally and theoretically to assess whether this technique would be useful for divertor heat flux control on NSTX-U.

References

[BP-1] S.J. Zweben et al, Phys. Plasmas 17, 102502 (2010)
[BP-2] Y. Sechrest et al, Phys. Plasmas 18, 012502 (2011)
[BP-3] R.J. Maqueda et al, "Intermittency in the scrape-off layer of NSTX during H-mode confinement", J. Nucl. Mat. (2010), in press.
[BP-4] D.A. Russell et al, Phys. Plasmas 18, 022306 (2011)
[BP-5] J.R. Myra et al, Phys. Plasmas 18 012305 (2011)
[BP-6] R.H. Cohen and D.D. Ryutov, Nucl. Fusion 37, 621 (1997)
[BP-7] S.J. Zweben et al, Plasma Phys. Cont. Fusion 51 105012 (2009)

Energetic Particle Research

Energetic Particles research in FY2011 focused primarily on three classes of instabilities associated with fast ion loss and redistribution: (i) high-frequency Alfvénic instabilities (CAE/GAE), (ii) TAE modes and (iii) low-frequency kink/fishbone modes.

Once de-stabilized, CAE/GAE modes can be responsible for radial redistribution of fast ions. Evidence has been found in an anomalous *High-Energy Feature* (HEF) observed on NPA spectra during strong high-f activity (Figure EP-1) [EP-1], which can be explained by the redistribution of fast ions caused by resonant GAE modes [EP-2, 3]. Modeling is also in progress to understand the effects of GAE/CAE modes on fast ion transport. Mode structures obtained with the HYM code are used in the newly developed, full-orbit particle following code SPIRAL [EP-4] to infer redistribution of fast ions. Results from HYM will be validated against measurements of the mode structure and frequency. GAE and CAE mode structures have been measured for the first time [EP-5] in the core of high-power (6 MW) beam-heated H-mode plasmas (Figure EP-2), in which enhanced electron thermal transport has been observed to correlate with high frequency AE activity [EP-6]. The CAE structure is strongly core-localized, indicating that both CAE and GAE modes are candidates for causing the enhanced thermal transport.

At lower frequency, the study of TAE avalanches and associated fast ion losses has continued for both L- and H-mode NSTX plasmas [EP-7, 8]. TAE structure has been measured with greatly

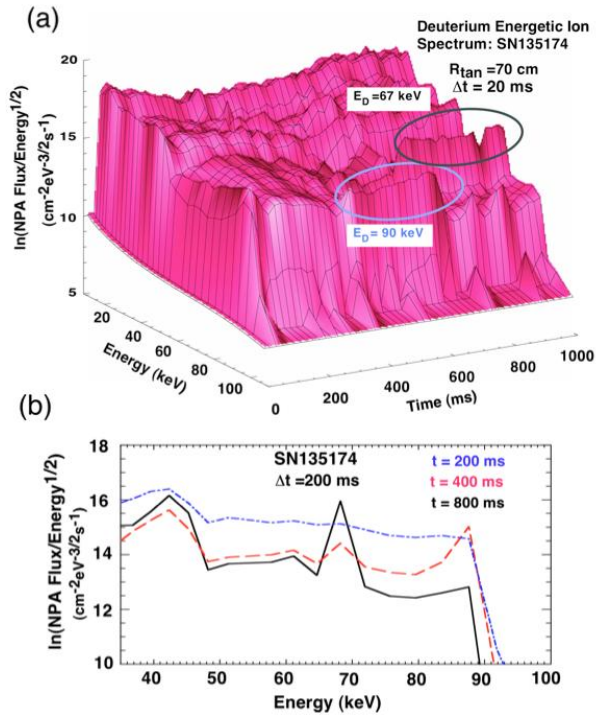

Figure EP-1: *(a) NPA spectrum showing "dual-energy" HEFs that appear as persistent flux increases localized around the NB full injection energies. (b) 2D energy spectra at selected times showing details of the dual-energy HEF flux increase.*

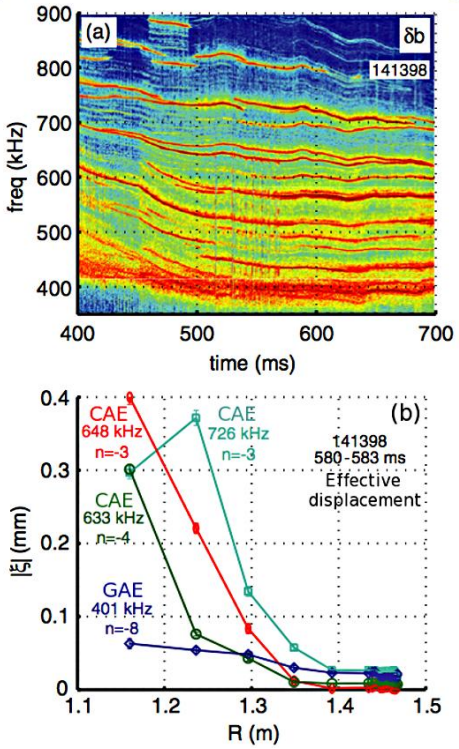

Figure EP-2: *(a) Spectrum from Mirnov coils showing CAE/GAE activity and (b) radial mode structure for the dominant CAE and GAE mdoes measured through a multi-channel reflectometer system.*

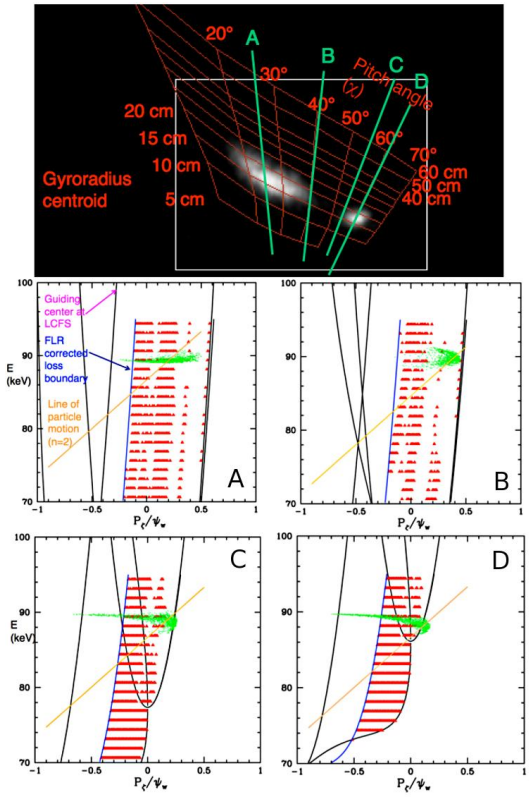

Figure EP-3: *(Top) sFLIP frame showing losses of fast ions with different pitch. (Bottom) ORBIT calculation of stochastic regions (red dots) for the four values of pitch in the upper frame (A-D). White regions inside the LCFS curves indicate confined orbits. Green dots are the deposited fast ions for the full-energy NB component.*

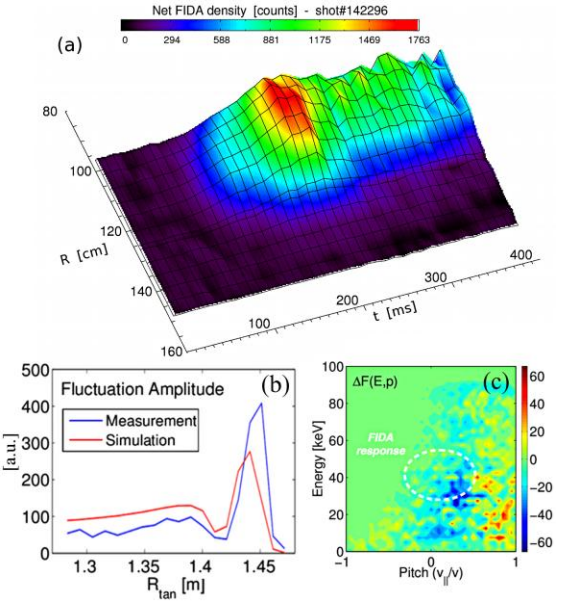

Figure EP-4: *(a) FIDA profile showing depletion caused by a kink mode after t~220 ms. (b) Measured and simulated profile of mode amplitude. (c) Fast ion distribution response to the kink as calculated by SPIRAL. The drop is ~20% in the region where the FIDA sensitivity is largest (dashed circle).*

improved spatial sampling. Measurements of the TAE phase show strong radial variation near the midplane, indicating radial propagation caused by non-ideal MHD effects [EP-5]. The guiding-center code ORBIT has been used to calculate the stochastic loss regions associated with multi-mode TAE *avalanches* (Figure EP-3). The mode structure used in ORBIT has been obtained by selecting ideal eigenmodes from the NOVA code based on reflectometer measurements [EP-7]. The phase-space response of the scintillator Fast Ion Loss Probe (sFLIP) has been included in the model. Results indicate that the fast ion losses observed on sFLIP as a function of energy and pitch are consistent with a stochastization of the fast ion phase- space induced by multiple TAE modes.

According to recent analyses [EP-9], TAE avalanches are also responsible for triggering low-frequency kink/fishbone modes, possibly through non-linear mode-mode coupling. The coupling process has been documented in L-mode plasmas. Simulations with the ideal MHD code NOVA support the interpretation of kink-like modes de-stabilized by the avalanche. More extensive studies have been performed for H-mode plasmas [EP-10], where kink-like modes are observed at the beginning of the current flat-top. FIDA and neutron rate measurements indicate a redistribution of fast ions following the appearance of these modes (Figure EP-4a). PEST simulations confirm that kink modes are unstable for these plasma conditions. The mode structure from simulations of the SXR response (Figure EP-4b) is then used in SPIRAL to simulate the response of the fast ion distribution to the instability [EP-4]. Preliminary results from SPIRAL indicate a redistribution of fast ions to larger pitch values. This is consistent with the observed drop in the measured FIDA profile, which is mainly sensitive to fast ions with small pitch values (Figure EP-4c).

References

[EP-1] S. S. Medley et al., submitted to Nucl. Fusion (2011)
[EP-2] S. S. Medley et al., PPPL Report no. 4652 (2011)
[EP-3] Y. Kolesnichenko et al., 12th IAEA-TM on Energetic Particles, Austin TX (2011), P-1.15
[EP-4] G. Kramer et al., 12th IAEA-TM on Energetic Particles, Austin TX (2011), P-1.18
[EP-5] N. Crocker et al., Plasma Phys. Control. Fusion **53** (2011) 105001
[EP-6] D. Stutman et al., Phys. Rev. Lett. **102** (2009) 115002
[EP-7] D. Darrow et al., 12th IAEA-TM on Energetic Particles, Austin TX (2011), O-1
[EP-8] E. Fredrickson et al., 12th IAEA-TM on Energetic Particles, Austin TX (2011), P-7
[EP-9] M. Podestà et al., 12th IAEA-TM on Energetic Particles, Austin TX (2011), I-3
[EP-10] A. Bortolon et al., 12th IAEA-TM on Energetic Particles, Austin TX (2011), O-12

High Harmonic Fast Wave Research

The Effect of ELMs on HHFW Heating of NBI Generated H-modes

ELMs reduce the stored energy achieved with HHFW heating compared with the ELM free case as also occurs for NBI heating alone [RF-1]. This reduction can be attributed both to direct ELM ejection of stored energy and to an increase in edge density with ELMs that exceeds the onset density for perpendicular wave propagation near the antenna [RF-2,3], and leads to significantly more edge RF power deposition. This latter effect causes a more intense RF "hot" zone spiral in the lower divertor scrape off region due to an increase in edge RF power propagating to the divertor from the antenna scrape off layer (SOL) region along the magnetic field lines. Fast IR measurements of the direct ELM heat deposition at the lower divertor [RF-4] shows it to be peaked in the vicinity of the outer strike radius and to fall off strongly as the "hot" zone is approached, indicating little direct ELM effect on the "hot" zone heating (Figure RF-1). This is an important result in that it indicates that the RF power need not be reduced during ELMs in order to prevent excessive direct ELM heating in the "hot" zone.

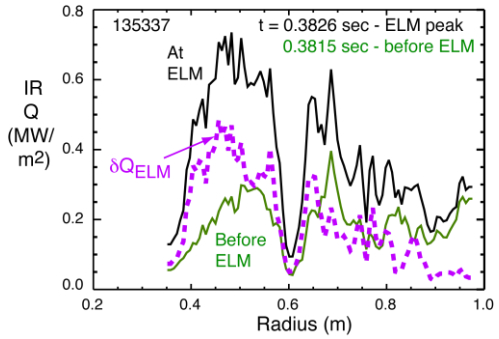

Figure RF-1: *Heat flux to the lower divertor plate due to the ELM at 0.3826 sec.. [$k_{||}$ = -13 m^{-1}/ϕ_{Ant} = -150°, D_2, P_{NB} = 2 MW, I_P = 0.8 MA/ B_T = 4.5 kG.] (see Ref RF-1)*

It is important to establish the physics properties of the "hot" zone in order to definitively establish the cause(s) of the heat flux deposition there for benchmarking advanced RF codes that can be used to predict such RF edge heating effects in ITER. Surface wave propagation in the SOL from the antenna region to the divertor region resulting in sheath rectification at the outer divertor plate is the most likely cause. However, it is also possible that dc electron currents produced by the antenna near fields could cause such heating. First measurements on NSTX at the RF "hot" zone spiral are the currents collected by instrumented divertor tiles [RF-5] shown in Figure RF-2. In Figure RF-3a the "hot" zone spiral is moved toward smaller radius R by increasing the magnetic field pitch (increasing I_P and decreasing B_T) to sweep the "hot" zone over the row 3 divertor tiles (R = 0.85 m to 0.95 m). As indicated in Figure RF-3b the currents at Bays I and K (see Figure RF-2) track the location of the spiral. Also, no current is detected in the row 3 tile at Bay G (see Figure RF-2) which is outboard of the spiral location. These results are a good indication that the RF interaction effects on the divertor plate are localized to the "hot" zone and probably associated

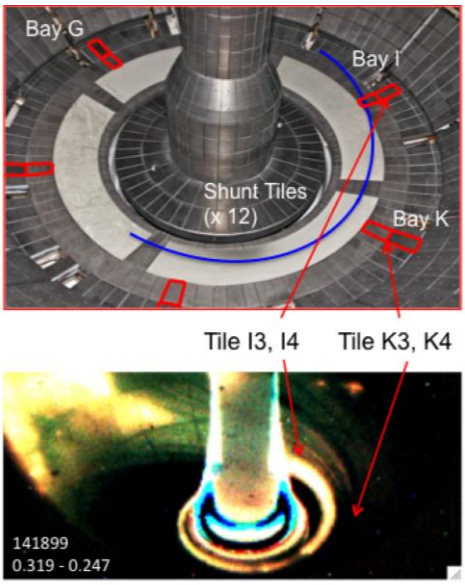

Figure RF-2: *Instrumented divertor tiles and the location of the RF "hot"zone spiral relative to them for shot 141899 at 0.319 sec.. ($k_{||}$ = -8m^{-1}/ϕ_{Ant} = -90°, D_2, P_{NB} =2 MW.)*

with RF fields. Further investigation of the actual RF fields in the "hot" zone is required to definitively determine the RF process involved.

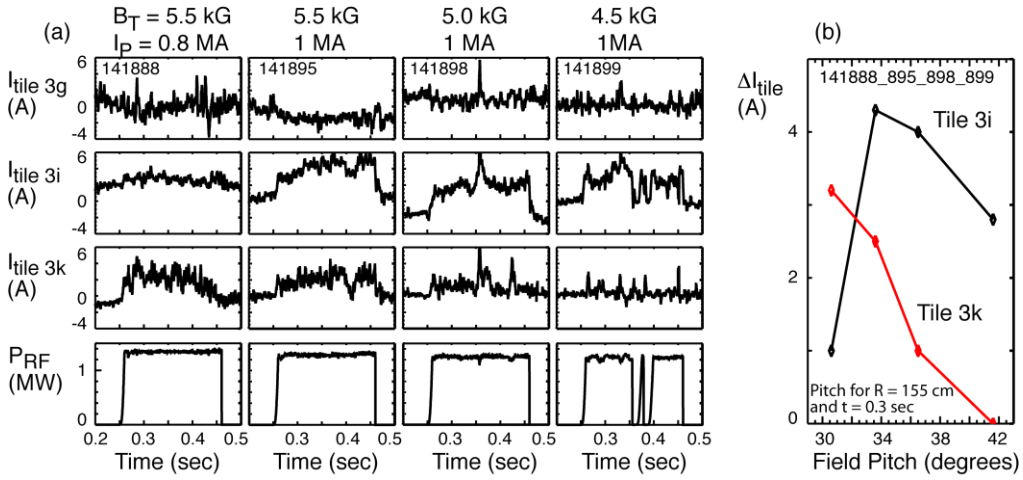

Figure RF-3: *(a) Row 3 divertor tile currents at Bays G, I and K versus 4 ratios of I_p/B_T. (b) Tile 3i and 3k currents versus field pitch in front of the antenna. ($k_{||} = -8m^{-1}/\phi_{Ant} = -90°$, D_2, P_{NB} =2 MW.) [see Reference RF-1]*

High non-inductive fraction HHFW-generated H-mode plasmas

The initial approach to developing fully non-inductive plasma current ramp-up in NSTX has been to heat during the flat top of a low plasma current $I_p \sim 300$ kA, $B_T = 5.5$ kG, ohmically-heated, deuterium plasma with 30 MHz high-harmonic fast wave (HHFW) power [RF-6], using a launched toroidal mode number, $k_\phi = -8\ m^{-1}$ (current drive antenna phasing), in order to drive the plasma into an H-mode with a non-inductive current fraction, $f_{NI} \geq 1$.

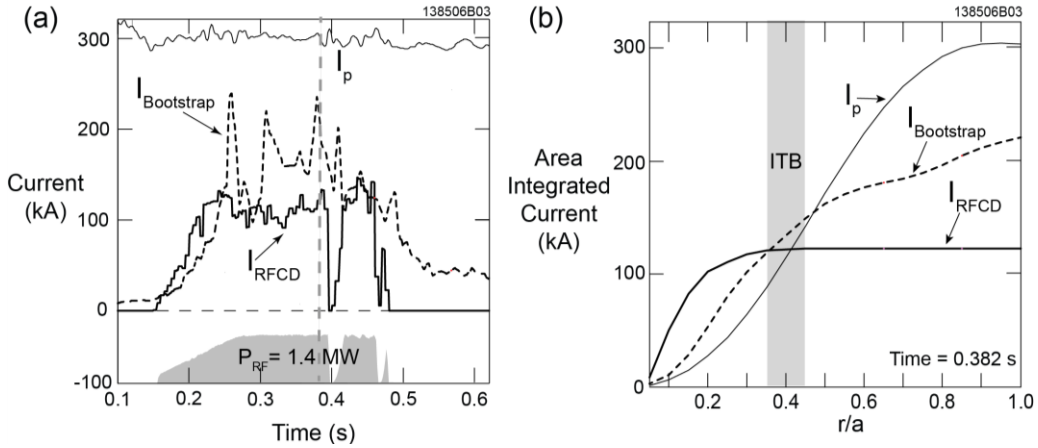

Figure RF-4: *TORIC full wave simulation results for shot 138506, assuming η_{eff} = 100%. (a) Time evolution of I_p (thin solid line), I_{RFCD} (thick solid line) and $I_{Bootstrap}$ (dashed line) and the RF power waveform (grey shading). (b) Area integrated current versus normalized minor radius at 0.382 s, the time indicated by the vertical dashed gray line in (a).*

When 1.4 MW of HHFW power was coupled into an I_p = 300 kA, B_T = 5.5 kG plasma (shot 138506), the central electron temperature $T_e(0)$ increased from 0.3 to 3 keV, and the electron density profile $n_e(R)$ developed a steep edge pedestal characteristic of the H-mode, and eventually a hollow core inside an internal transport barrier (ITB) that developed at r/a ~ 0.4. In FY2011, the time evolution of the RF current drive (I_{RFCD}) and the bootstrap current ($I_{bootstrap}$) were modeled with a version of the TORIC full-wave code [RF-7] that is integrated into the TRANSP transport code [RF-8]. Modeling was performed assuming the RF coupling efficiency, η_{eff} = 100%, and some of the results are shown in Figure RF-4. I_{RFCD} reaches 120 kA (Figure RF-4(a)) and is entirely driven within the ITB (Figure RF-4(b)). 60% of the bootstrap current ($I_{Bootstrap}$) is driven inside the ITB (Figure RF-4(b)). $I_{Bootstrap}$ fluctuates between 100 and 200 kA (Figure RF-4(a)) as the pressure gradient near the ITB changes. These model results predicts f_{NI} ~ 1, but from the rise in stored energy and the energy confinement time, η_{eff} is estimated to be only ~ 60%, yielding f_{NI} ~ 0.65. HHFW power could not be increased above 1.4 MW during these experiments due to poor antenna conditioning. However, previously > 2.5 MW of k_ϕ = -8 m^{-1} of HHFW has been successfully coupled into a helium HHFW-generated H-mode at I_p = 650 kA [RF-9], so there is enough HHFW power available on NSTX to generate $f_{NI} \geq 1$ in an I_p ~ 300 kA plasma.

Comparison of TORIC Simulations of HHFW Heating with Experimental Measurements

Direct comparisons of predictions of the HHFW field and power deposition profiles against NSTX data are difficult in part because of the lack of diagnostics which can directly measure these quantities. Diagnostics designed to measure wave induced fluctuations, such as the reflectometers or the high-k scattering system, are not yet equipped to detect signals in the 30 MHz range of the HHFW's. Furthermore, because of the over-dense nature of the NSTX plasmas, continuous time-resolved diagnostics, based on electron cyclotron emission, of the electron temperature and density cannot be used to infer the HHFW power deposition via the response of a time-modulated applied HHFW power. Previously, the volume – integrated power absorbed in the plasma from HHFW heating has been inferred by fitting an exponential function to the rise or fall in total stored energy measured with magnetic reconstructions or else electron stored energy measured with Thomson scattering at the turn-on and turn-off times, respectively, of an HHFW pulse [RF-2]. This technique was extended over the past year to utilize a rolling volume integration of the change in measured electron stored energy to infer the local HHFW electron power despoition profile as a function of normalized minor radius, ρ=r/a [RF-10]. As shown in Figure RF-5, the

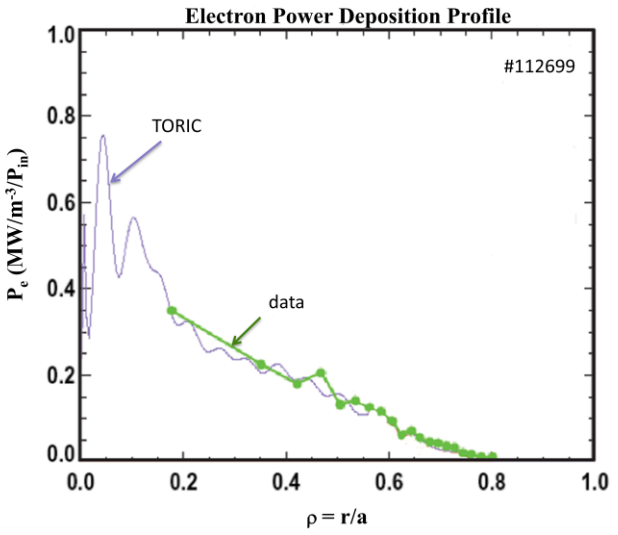

Figure RF-5: *The electron power deposition profile inferred from the time evolution of the electron stored energy measured with Thomson scattering is compared to the prediction from the TORIC code. Both profiles have been normalized assuming 1 MW of input power.*

inferred radial electron power deposition profile, normalized to the total volume integrated power, from this extended data analysis agrees reasonably well with the prediction from TORIC in an NSTX discharge (shot #112699) in which the antenna phasing was set to 180˚, at least for $\rho > 0.2$. It was found to be difficult to fit an exponential curve to the time evolution of electron stored energy at smaller minor radii, because the exponential time constants tend to be very long in this region and hence the fits are more sensitive to small changes in the measured stored energy. For discharges with current drive phasing (-90˚), it was possible to infer the electron power deposition profiles only for $\rho > 0.5$. Nevertheless, the agreement in the initial comparisons between the code predictions and the measurements indicates that the wave models in TORIC provide a good model for the core HHFW electron power deposition. It should be noted that the overall coupling/heating efficiency in the shot used in Figure RF-5 was only about 35% due to edge losses associated with surface waves and other parasitic effects. Subsequent optimization of the edge density profile (via increased D pumping by lithium wall coatings) combined with increased toroidal field was shown to reduce the edge losses and substantially increase the coupling efficiency in both heating and current-drive phasings as reported previously (and in references below).

References

[RF-1] J.C. Hosea *et al.*, RF Conference (Strasbourg 2011), to be published in *AIP Conf Proceedings.*

[RF-2] J.C. Hosea *et al., Physics of Plasmas* **15** (2008) 056104.

[RF-3] C.K. Phillips *et al., Nuclear Fusion* **49** (2009) 075015.

[RF-4] J-W. Ahn *et al., Review of Scientific Instruments* **81** (2010)

[RF-5] S. Gerhardt *et al., to be published.*

[RF-6] G. Taylor, *et al*., 38th EPS Conf. on Plasma Physics, Strasbourg, France (2011) - P5.095.

[RF-7] M. Brambilla, *Plasma Phys. Control. Fusion* **44**, 2423 (2002).

[RF-8] R. J. Hawryluk, in *Physics of Plasmas Close to Thermonuclear Conditions*, *Proc. of the International School of Plasma Physics*, (Pergamon, Varenna, Italy, 1981), Vol. 1, p. 1.

[RF-9] J. C. Hosea, *et al*., 38th EPS Conf. on Plasma Physics, Strasbourg, France (2011) - P2.098.

[RF-10] L. Berk et al, "HHFW Heating Efficiency and Spatial Power Deposition Profiles on NSTX", BAPS.2010.DPP.JP9.76

Scenario modeling and vertical stability calculations in preparation for NSTX-U

In preparation for NSTX-U operation and to provide a wide range of reference plasma scenarios for simulating and projecting physics in NSTX-U, an expanded study of the NSTX-U equilibrium operating space was performed using the free-boundary TRANSP code. The goal of these studies was to identify interesting fully-relaxed scenarios with $q_{min} > 1$ satisfying various programmatic goals, and to study the effects of thermal profile shape and confinement variations on those scenarios. In particular, comparisons between the ITER-98 scaling law and an ST specific scaling law with significantly stronger B_T and weaker I_P dependencies has been investigated.

A summary of these results is shown in Figure ASC-1, where the various fully relaxed profiles are shown; these include the electron temperature and density profiles, the neutral beam, bootstrap and Ohmic current density profiles, and the safety factor profiles. All calculations shown here assume (neo)classical fast ion physics and Z_{eff}=2. The Greenwald fraction is between 0.7 and 0.75 for all cases. The target plasma boundary for the free-boundary calculation has aspect ratio 1.75 and elongation of 2.8.

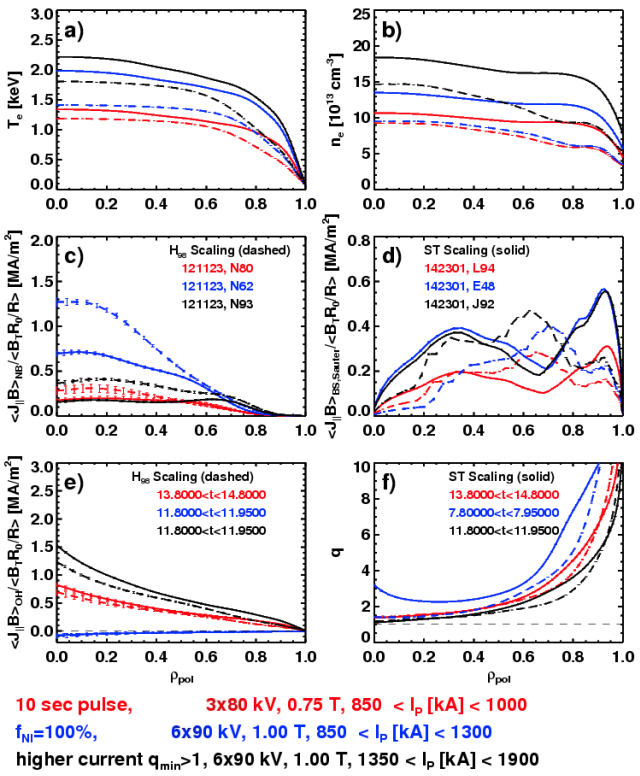

Figure ASC-1: *Profiles of (a) electron temperature, (b) electron density, (c) NBI-driven current density, (d) bootstrap current density, (e) inductively-driven current density, and (f) safety factor for ITER ELMy H-mode confinement scaling (dashed) and ST confinement scaling (solid)*

The red curves correspond to a configuration optimized for very long pulse length. The neutral beams are configured to 80 kV injection energy, and are modulated so that i) a 10 second pulse with 5.1 MW of input power can be achieved with each source on for only 5 seconds, and ii) there are minimal safety factor temporal variations. For the more narrow thermal profile assumptions and taking the ITER-98 scaling on the thermal confinement (dashed line), a 10 second pulse can be achieved at 850 kA. Assuming broadened profiles, combined with the ST confinement scaling assumptions (solid line), result in 1100 kA plasma current sustainment level. The current level in both cases is set by the need to not exceed the Ohmic heating limit of the solenoid coil during 10 second pulses. The central safety factor is consequently somewhat elevated, which should enhance the global stability of the configurations.

The blue curves correspond to an optimization of the non-inductive current level for B_T = 1.0T and 12.6 MW of injected power. Once again the dashed curves show the results for more peaked kinetic profiles and ITER-98 scaling. The non-inductive current level in this case is 850 kA. The

solid curves illustrate the more favorable ST confinement scaling with broader profiles. These yield a non-inductive current level of ~1300 kA, with q_{min}>2 across the entire plasma.

The final optimization in black shows cases with the highest possible current consistent with q_{min} > 1, again with 12.6 MW of input power and a toroidal field of 1.0 T. The less favorable peaked profiles and ITER-98 confinement scaling (dashed line) predict a sustainable current level of 1350 kA. The more favorable profiles and ST confinement scaling predict fully relaxed q_{min}>1 profiles for I_P=1900 MA. The central electron temperature exceeds 2 keV and the total stored energy exceeds 1.2 MJ in these scenarios. This level of stored energy, in principle sustainable for nearly 3 seconds with 90kV injection energy, is nearly three times larger than that transiently achieved in NSTX.

These and other studies illustrate a number of important features regarding NSTX-Upgrade equilibria. A range of safety factor profiles should be accessible in fully relaxed plasmas, facilitating important research into the interaction between transport, stability, and the current profile. There are significant differences in the current equilibrium configurations for the ITER-98 and ST thermal confinement scaling assumptions, and it should thus be possible to clearly resolve which scaling has the correct trends at higher field and current. Finally, the 10 second pulse scenarios should allow important studies of such facilitate disparate topics as disruption avoidance or long pulse particle control.

The scenario modeling described above assumes that NSTX Upgrade will be capable of reliably achieving increased elongation at increased aspect ratio. As described in the summary for milestone R11-2, preliminary experimental data from NSTX shows that higher aspect ratio will have higher VDE growth rates, and thus control of the vertical instability will be more difficult. In order to quantify this effect and develop sufficient vertical control capability for NSTX-U, improved modeling capability is being pursued. The NSTX vertical control model presently being tested is the "Toksys" linear plasma model developed by General Atomics. The code is now operational and testing of the NSTX model for Toksys with the experimental data is in progress. Further, the NSTX PCS was modified to enable freezing of the voltage request in the Isoflux boundary control algorithm to enable uncontrolled plasma vertical drift and growth rate measurements to test the plasma models against experimental data. Figure ASC-2 shows experimental VDE growth rates compared to predictions, and the trend of increased growth rate with increased aspect ratio is evident for both the data and the model. Present research is focused on determining the cause of the factor of 2 discrepancy between measurement and model evident in Figure ASC-2. Possible causes include: non-linear vertical drift growth-rates and/or insufficient plasma and/or passive conductor models.

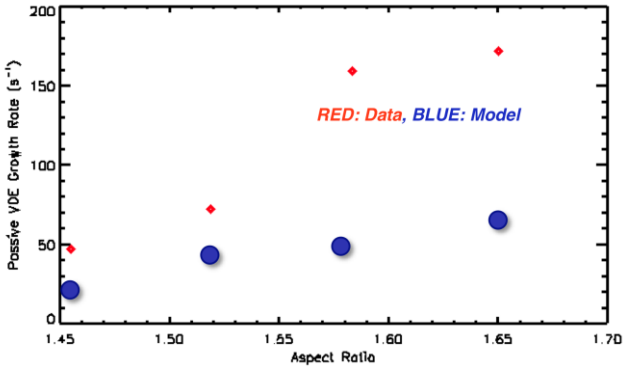

Figure ASC-2: *Measured vertical growth data (red, diamond) and Toksys model predictions (blue, circle) for a range of aspect ratios spanning NSTX and NSTX-U values (based on shots 141639-141642).*

NSTX Research in Support of ITER

Halo current dynamics

NSTX has completed experiments and analysis designed to understand the dynamics of "halo currents" during disruptions. These are currents that flow, during a disruption, through the edge plasma, into and through in-vessel components, and then back into the plasma. The parts of these currents flowing in the vessel and crossing the strong toroidal field can cause significant mechanical loading on those components. Furthermore, if the currents are toroidal localized, the resulting forces are concentrated; if the pattern rotates toroidally, mechanical resonances can amplify the destructive effect. This is a significant concern for ITER, where slowly rotating halo currents can interact with ~1 Hz vessel resonances.

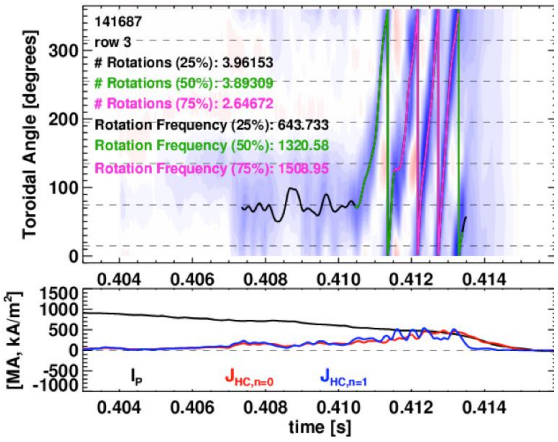

Figure ITER-1 *- (top) Contour plot of the halo current flowing into the vessel floor as a function to time and toroidal angle, and (bottom) time history of the plasma current and n=0 & 1 components of the halo current. The lines in the top frame show the reconstructed phase of the toroidal non-axisymmetry.*

NSTX was instrumented with an array of 12 specially instrumented tiles in the lower outboard divertor (six tiles in each of two rows); resistive shunts under these tiles allow the halo current flowing into the tiles to be measured. An example of these measurements is shown in Figure ITER-1 where the upper-frame shows the halo current flowing into the divertor as a function of time and toroidal angle. The halo currents begin to flow at t=0.407 s, a few ms after the start of the current quench. The pattern begins to rotate toroidally at ~t=0.415 s, with a rotation frequency during the period of maximum rotation of ~1.5 kHz. We also note that the halo current pattern is non-axisymmetric from early time, with the n=1 (toroidally asymmetric) component comparable in strength to the n=0 (axisymmetric) part. However, for t>0.4135, at the tail end of the current quench, the current pattern becomes quite toroidally symmetric. Magnetics modeling indicates that the last closed magnetic surfaces may have vanished at this time, leaving behind a toroidally symmetric halo current.

NSTX has also begun a parametric analysis of the conditions that lead to significant halo current rotation in NSTX. Two important observations are shown in Figure ITER-2. The left frame of the figure shows the rotation frequency plotted against the plasma current quench rate. It is clear that the cases with most rapid rotation are those with slow I_P quenches. This implies that, for NSTX-like conditions, the worst mechanical loading from halo current rotation is unlikely to be superimposed on the largest eddy current loading. The second frame shows the rotation

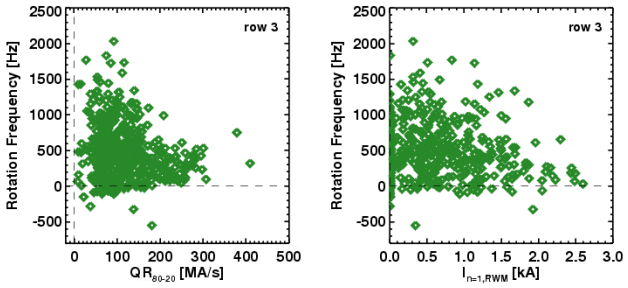

Figure ITER-2 *- Plots of the halo current n=1 asymmetry rotation frequency as a function of the (left) the plasma current quench rate and (right) the n=1 applied field amplitude.*

frequency as a function of the applied n=1 field and indicates that it may be possible to modify halo dynamics using non-axisymmetric fields, though the required fields appear to be large.

Disruption Mitigation

Predicting and controlling disruptions is an important and urgent issue for ITER. Reactors based on the ST and Tokamak concepts are expected to carry many MA of plasma current and therefore have the potential for disruption and the generation of substantial amounts of run-away electrons. While work is in progress to avoid disruptions, some may be unavoidable. For these cases, a fast discharge termination method is needed to minimize the deleterious effects of the disruption.

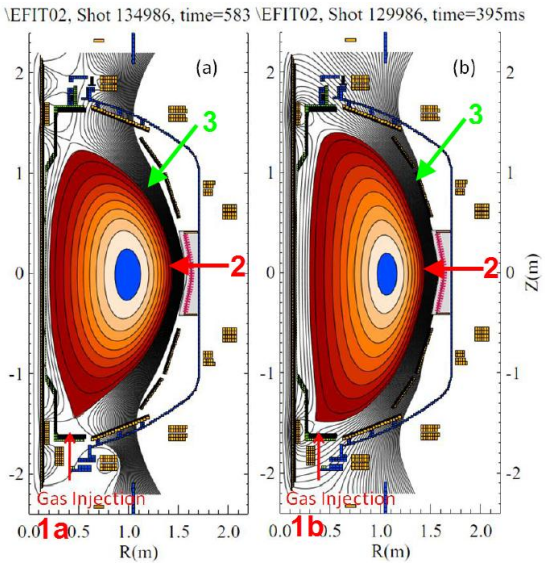

Figure ITER-3 *- Shown are the planned Massive Gas Injection locations on NSTX-U. (1a)-Private flux region, (2)-Conventional mid-plane injection, (1b)-high field lower scrape-off-layer region and (3) above mid-plane.*

At present Massive Gas Injection (MGI) is the most promising method for safely terminating discharges in ITER. Recent experimental results have shown that the cold front from the edge, which has been cooled by a massive gas injection pulse, needs to reach the q=2 surface for the onset of rapid core cooling to occur. On ITER, because of the large minor radius of the device, the long transit times for the slow moving neutral gas, and the large scrape-off-layer flows, it is not known if a simple MGI pulse from multiple locations would be adequate. Insight into ways for reducing the total amount of injected gas and optimizing the injection locations would further help with the design of a reliable system for ITER. NSTX Upgrade will offer new data by injecting gas into the private flux and lower x-point regions to determine if this is a more desirable location for massive gas injection.

Injection from this new location has two advantages. First, the gas is injected directly into the private flux region, so that it does not need to penetrate the scrape-off-layer. Second, because the injection location is located near the high-field side region, the injected gas should be more rapidly transported to the interior as known from high-field side pellet injection research performed on other devices, and from high-field side gas injection on NSTX. By comparing gas injection from this new location to results obtained from injecting a similar amount of gas from the conventional outer mid-plane, NSTX Upgrade results on massive gas injection will provide additional insight, a new database for improving computational simulations, and additional knowledge to disruption mitigation physics using massive gas injection.

At present two massive gas injection assemblies have been installed and commissioned on NSTX that will also be installed on NSTX Upgrade. Of particular interest is the comparison of injection location (1a) with location (2) as shown in Figure ITER-3.